RESEARCH ARTICLE

Geoarchaeology An International Journal WILEY

Linking archaeology and paleoenvironment: Mid-Holocene occupational sequences in the Varamin Plain (Iran)

Robert Busch[1] | Reinhard Bernbeck[2] | Morteza Hessari[3] | Fabian Kirsten[1] | Christopher Lüthgens[4] | Susan Pollock[2] | Nolwen Rol[2] | Brigitta Schütt[1]

[1]Institute of Geographical Sciences, Freie Universität Berlin, Berlin, Germany

[2]Institute for Near Eastern Archaeology, Freie Universität Berlin, Berlin, Germany

[3]Cultural Heritage and Tourism Research Institute, Tehran, Iran

[4]Institute of Applied Geology, University of Natural Resources and Life Sciences, Vienna, Austria

Correspondence
Robert Busch, Institute of Geographical Sciences, Freie Universität Berlin, Malteserstraße 74-100, 12449 Berlin, Germany.
Email: robert.busch@fu-berlin.de

Scientific editing by Sarah Sherwood.

Abstract

Early human habitation of the arid to semiarid Central Iranian Plateau was strongly connected to the availability of water and associated natural hazards, such as flooding and drought events. In this geoarchaeological study, we focus on the occupation at the prehistoric site of Ajor Pazi within the formerly active fluvial environment of the Varamin Plain. Through radiocarbon and luminescence-dated sediment cross-sections, we apply multivariate statistics to sedimentological characteristics of bulk samples collected during a rescue excavation in 2018. Based on facies interpretations, we differentiate depositional processes and present their implications for the environs of Ajor Pazi. Our results show evidence of settlement activities between 6.4 and 5.6 ka cal B.P. (4.4–3.6 ka cal. B.C.E.). Phases of reduced geomorphodynamics can be distinguished when soil-forming processes take place. Our findings provide insights into the hitherto scarcely explored Transitional Chalcolithic II period during which the site of Ajor Pazi emerged and began to shape its environs.

KEYWORDS
alluvial fan, geomorphology, landscape archaeology, mid-Holocene

1 | INTRODUCTION

The development of early human societies and the associated expansion of managed environments have been affected by climatic variability and have led these societies to adapt to changing ecosystems in the Holocene. Water availability represents a common determinant of settlement location, both in cases of continuous and noncontinuous human habitation (Valipour et al., 2020). With the onset of crop cultivation and increasing sedentism, the importance of access to a permanent water supply grew. This applies especially to the drylands of the Fertile Crescent and neighboring areas, which were the heartland of early sedentism and crop cultivation. Wherever local climate was characterized by a negative water balance, settlement activity took place where perennial streams or springs provided year-round water for household and irrigation needs. In the arid to semi-arid Iranian highlands, a concentration of prehistoric settlements on alluvial fans and in the vicinity of perennial river systems can be observed, for example, in the forelands of the Alborz mountains (Jackson, 2006; Meder, 1979; Schmidt et al., 2011). Besides the water supply, the alluvial fan sediments provided fertile soils and raw materials for pottery production and domestic architecture (Jackson, 2006; Maghsoudi et al., 2014). Nonetheless, the basis of subsistence was coupled with the unpredictable risk of episodic, extreme runoff events, droughts, and—in the case of the Iranian highlands—tectonic activities. The adaption and resilience of former societies to such natural hazards was an essential factor for the continuous inhabitation of such settlements (Knitter et al., 2021).

A good example of the agreement between settlement-limiting risk exposure and suitable land use conditions is found on the Jajrud alluvial fan in the northern highlands of Iran. The Jajrud river (*rūd* Persian for river) is one of the major streams draining the Anti-Alborz mountains (Figure 1). After emerging south from the Anti-Alborz, the Jajrud river forms a large-scale Plio-Pleistocene alluvial fan where the current city of Varamin is located—and which is commonly named Varamin Plain. In our study, we focus on the Mid-Holocene occupational sequences in the Varamin Plain, where archaeological surveys by M. Hessari and a team from the Iranian Center of Archaeological Research (Hessari et al., 2014), as well as work by other researchers (e.g., Fazeli et al., 2007) have led to the discovery of ca. 230 settlement sites (Pollock et al., 2023). Intensive agricultural usage of the Jajrud alluvial fan, including substantial earth movements in the most recent decades as part of the industrialization of agriculture as well as clay quarrying, caused major destruction of archaeological sites.

The study focuses on the archaeological site of Ajor Pazi (35°15′ 5″N, 51°43′25″E) southeast of the modern city of Varamin (Figure 1). The site is located in a clay quarry and contains numerous finds and several thin occupational layers dating to prehistoric times. We use the descriptions and samples collected during an archaeological rescue excavation in a clay pit in 2018 to better understand the environmental history of the settlement location. Our primary aim is to differentiate occupational phases and distinguish them from hiatuses by applying multivariate statistics on sedimentological characteristics of samples collected according to archaeological sampling strategies. Feldspar luminescence dating and radiocarbon (C14) dating are applied to set the temporal frame of the prehistoric settlement through numerical dating.

1.1 | Natural setting

Ajor Pazi is located in the southeastern Varamin Plain, about 6 km south of the town of Pishva and ca. 55 km southeast of Tehran (Figure 1). Geologically, the site is located south of an intermontane basin between the Parchin fault in the north, the Pishva fault in the
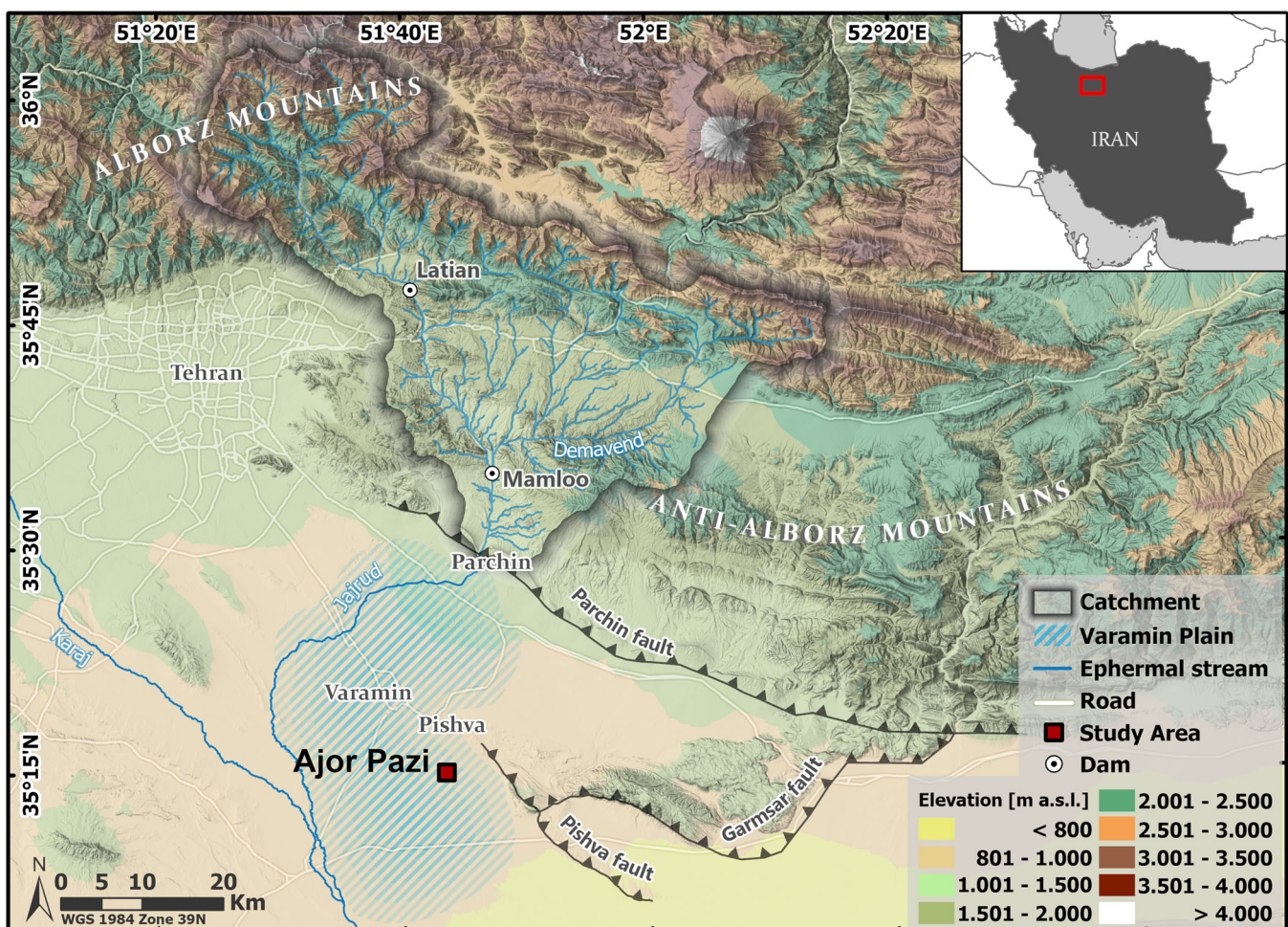
FIGURE 1 Regional overview. Multidirectional hillshade and elevation (in meters above sea level) map of the study area and the surroundings using the GLO-30 DSM, © DLR e.V. and © Airbus Defence and Space GmbH (2018) provided under COPERNICUS by the European Union and ESA. Thrust fault lines are digitalized from the Geological Map of Varamin (Sadeghi & Fondoudi, 2006) and extended after Abbassi et al. (2010). Ephemeral streams within the Jajrud catchment are delineated from the GLO-30 DSM using ArcGIS Pro.

south, and the Garmsar fault in the east. The Parchin and Pishva faults dip NE and strike NW, with the Parchin fault forming the southwestern boundary of the Anti-Alborz Mountains. The Garmsar fault curves from W to E with a dipping to the NW (Figure 1).

The Varamin Plain is located on the alluvial fan of the Jajrud river, whose headwater area is in the Alborz and the Anti-Alborz mountains. Both mountainous areas are composed of Mesozoic calcareous formations and Miocene to Pliocene marly clastic rock formations (Sadeghi & Fondoudi, 2006). Emerging at the southern foothills of the Anti-Alborz, prograding deposits of the Jajrud river filled the intermontane basin since Plio-Pleistocene times and have formed a large-scale alluvial plain (ca. 1200 km^2) (Beaumont, 1968, 1972; Ridder & Erez, 1977).

The oldest fan deposits, the so-called Hazardareh beds, consist primarily of regular bedded sandy gravels and cover extensively the base of the intermontane basin (Ridder & Erez, 1977; Rieben, 1955), expanding even into the Tehran Plain in the northwest. The Jajrud river cuts through the Anti-Alborz close to Parchin, draining an area of approximately 1900 km^2. The Demavend river, coming from the east, forms the largest tributary of the Jajrud river with a drainage basin area of approximately 800 km^2.

The relief of the Jajrud river headwater area is mountainous and is characterized by elevations ranging from 4293 to 1131 m asl at the fan's apex from where it slowly declines to the fan's apron at approximately 800 m asl. At its outlet into the Varamin Plain, the Jajrud channel diverges into anastomosing branches, and its alluvial deposits form a fan within the plain. Fan deposits show typical sequences with coarse material around the apex and finer sediments downstream (Beaumont, 1968; Ridder & Erez, 1977). However, at Pishva, the transport of alluvial deposits has been deflected by the topographic uplift of the Pishva fault, which disrupts the fanning and causes a characteristic western offset of the plain (Figures 1 and 2). According to Ridder and Erez (1977), this offset is accompanied by a substantial accumulation of up to 300 m of Quaternary sediments between today's towns of Varamin and Pishva. As part of this process, the Pishva hill redirected the sediment flow of the fluvial system (Figure 2) and formed an accumulation spur toward the south (Ridder & Erez, 1977). The Great Kavir (*kavir* Persian for desert) is located in the southeastern proximity of the Jajrud river. Due to its playa-lake character, it forms an important origin for aeolian-transported
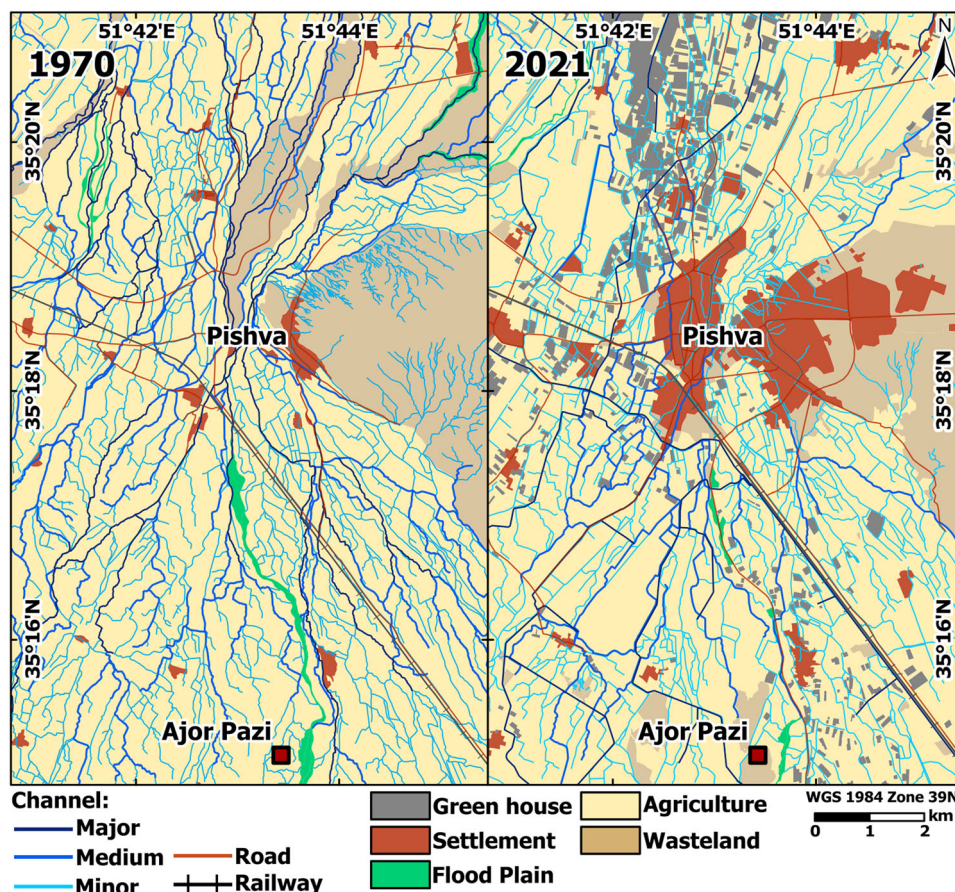
FIGURE 2 Overview maps of the study site of Ajor Pazi and surroundings. The channels shown are based on the bachelor thesis by Otto (2022), who visually identified and mapped water channels and land use using KH4B ("CORONA") satellite imagery taken on 31.05.1970. In comparison, recent land use and water channels were mapped using the "world imagery" basemap in ArcGIS (Esri, Maxar, Earthstar Geographics, CNES/Airbus DS, USDA, USGS, AeroGRID, IGN, and the GIS User Community), which included satellite imagery taken on 31.01.2021 and 21.02.2021.

material (Beaumont, 1972). At present, the Jajrud alluvial fan extends over a length of about 40 km.

The climate of the Varamin Plain is semi-arid continental. At the weather station in Tehran-Mehrabad (1191 m asl), the annual average temperature amounts to 18.2°C a^{-1}, and annual precipitation averages 262 mm a^{-1} (reference period 1991–2020; Menne et al., 2012). Most rainfall occurs between November and March. In contrast, a colder and more humid mountain climate prevails in the highlands of the Anti-Alborz, in the headwater area of the Jajrud river, with an annual precipitation between 580 and 720 mm a^{-1} (Jamshidi et al., 2010; Maghrebi et al., 2010). Since a major part of this precipitation is attributable to snowfall, a nival runoff regime characterizes the Jajrud river with a discharge peak during late spring (Razmkhah et al., 2009).

Soils of the Jajrud fan vary in type and development stage and are primarily characterized by clayey to silty-loamy textures with a relatively shallow depth (Beaumont, 1972; Ridder & Erez, 1977). In the upper to central part of the Jajrud fan, grayish-brown soils with irregular accumulations of calcretes and gypscretes predominate. In contrast, brown deep solonchak soils and salt crusts are more likely to be found in the southern (distal) part of the fan close to the Great Kavir (Beaumont, 1972; Bordbar, 1967; Ridder & Erez, 1977).

Human activities dominate current surface dynamics on the Jajrud fan. Since the construction of the Latian Dam in the 1960s at the break through the Anti-Alborz, runoff from the upper Jajrud catchment has been retained and used for Tehran's water supply. With the additional construction of the Mamloo Dam in 1970, at the outlet of the headwater area (Figure 1), the alluvial plain was completely disconnected from its source area (Beaumont, 1974). The natural drainage system of the alluvial fan was substantially modified to ensure the water supply of the city of Tehran. The rectification of main channels and their partial channelization provided a basis for further extensive melioration measures. The comparison of land use and channel network around Pishva between 1970 (KH-4 "Corona" optical satellite imagery) and 2021 shows a severe change in drainage density and, therefore, a reduction of bifurcations (Figure 2).

The branching river network around 1970 emphasizes the fluvial dynamics of the alluvial fan before the present-day adjustment of the fluvial system. Natural morphodynamics switched from fluvial-dominated, erosion-sedimentation sequences to an environment extensively controlled by humans. At present, brickmaking, large-scale cultivation of vegetables, land leveling for irrigation, well drilling, and the growth of urban-centers, such as Varamin and Pishva, have fundamentally transformed the landscape.

1.2 | The archaeological site of Ajor Pazi

In the Varamin Plain prehistoric settlements form only a small part of the total number of archaeological sites. Neolithic and Transitional Chalcolithic periods are overall poorly represented: 27 sites can be assigned to the following Chalcolithic period of the late fifth to mid-fourth millennium B.C.E. (Sialk III period). During the Early Bronze

Age (Sialk IV,1 and IV,2), also referred to as the Proto-Elamite period, the number of known sites in the research area diminished to five (Hessari et al., 2014) before the complete abandonment of the Varamin Plain until its resettlement during the Iron Age. The few known Neolithic and Transitional Chalcolithic (TC) settlements, such as Moeinabad (Hessari et al., 2014) or Tappeh Pardis (Fazeli et al., 2007), are mounded sites, implying lengthy periods of habitation, while the Chalcolithic and Early Bronze Age sites show only a few layers of settlement debris before being abandoned (Pollock et al., 2023).

Remains of the buried prehistoric site of Ajor Pazi have been found dispersed through several cross-sections in a large, deep pit in a privately owned brick factory. In 2013, at the time of the site's first discovery, an extensive heap of loose bulldozed material was found. Though not in situ, it included prehistoric sherds that could be assigned to various subperiods of the Chalcolithic, some as late as the Early Bronze Age (Ghasemi et al., 2018). The pile of shifted deposits was removed between 2014 and 2015. For that reason, all of the material could not be collected. The clay quarrying exposed cross-sections that displayed multiple archaeological contexts. Many others located between the standing cross-sections were likely completely destroyed, but a segment that contained numerous pebbles, which made it unsuitable for brickmaking, was left undisturbed. This undisturbed block has a height of 4 m, a length of 61 m striking NW–SE, and a width of 17 m (Figure 3). Northeast of the block, a 16-m-wide trench (Cut I) was created, striking NW–SE. Both sides of the cut revealed suitable cross-sections. The cross-section to the southwest of the cut is 61 m long (Southwest [SW] cross-section). At the time of fieldwork in 2018, the cross-section to the northeast of the cut had a length of ca. 400 m and was labeled "Main profile (MP)" (Figure 3). A third cross-section at the southwestern margin of the original block with the profile wall facing toward the northeast was labeled "Northeast (NE) cross-section" (Figure 3).

Today, the cross-sections have been almost destroyed, particularly the long Main Profile has been bulldozed for brick making. It is thus more than unfortunate that the brevity of our research at this important site prevented us from acquiring larger, contextually well-defined samples of pottery and other archaeological remains. The sole well-stratified materials from securely Transitional Chalcolithic II dated contexts stem from profiles in the form of cutbacks of the cross-sections (Figure 3). The extreme fragmentation of the material does not allow us to identify parallels to other sites in the region or beyond. Overall, reddish ceramic wares that can be attributed to a Transitional Chalcolithic II horizon are found throughout the extant profiles of Ajor Pazi (see Figure 3: up to a height of ca. 1.50 m above the ground surface in Cut I [a.g.s.] in profile B, 1.40 m a.g.s. in profile F, possibly up to 2 m a.g.s. in key-profile C), before the appearance of an increased number of plain buff and black-on-buff painted sherds characteristic of later Chalcolithic subperiods. The latter material is rarely found at Ajor Pazi in well-stratified contexts and is often mixed with pebbles (see also Ghasemi et al., 2018). Only a few of the pottery sherds are indicative of an ephemeral Early or Middle Chalcolithic (Sialk III, 1–5) occupation similar to those identified at nearby Chaltasian or Ahmadabad-e Kuzehgaran (Bernbeck et al.,
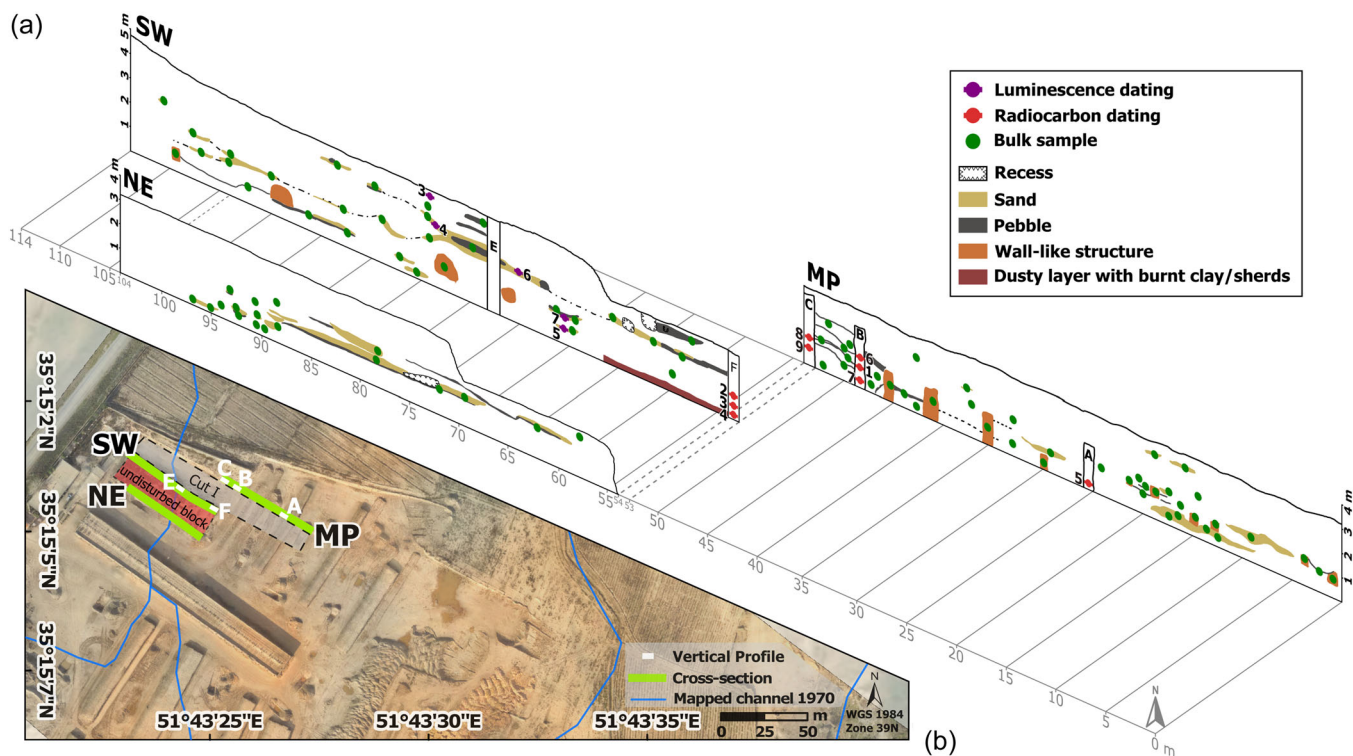
FIGURE 3 Overview derived from profile sketches of the NE, SW, and MP cross-sections. (a) Profiles indicated in their approximate extent (A, B, and C in section MP, D not included, E, F in section SW). Outstanding textural or archaeological features are marked; the untagged, white outcrop areas correspond to facies "(a)" as the sedimentological background. Bulk samples taken for sedimentological analysis are marked as green dots. (b) Spatial alignment of the cross-sections. The orthophoto was taken by M. Rokni (Iranian Center of Archaeological Research) in 2021. The background is based on the Firefly basemap in ArcGIS Pro (Esri, Maxar, Earthstar Geographics, CNES/Airbus DS, USDA, USGS, AeroGRID, IGN, and the GIS User Community).

2020; Rol et al., 2022), and as yet recorded exclusively from the area east of profile B (Figure 3a), at relative heights both similar to and higher than the Transitional Chalcolithic II.

2 | MATERIALS AND METHODS

2.1 | Sampling strategy

A survey conducted in July 2018 by R. Bernbeck, M. Hessari, and B. Schütt examined occupational remains at Ajor Pazi. Systematic cleaning and complete recording of the extensive cross-sections (NE, SW, MP) were not feasible during the sampling campaign in August–September 2018. Therefore, the sampling strategy was oriented along two different lines and followed the needs of an archaeological rescue excavation.

Six 1-m-wide profiles (A-F; Figure 3 and Supporting Information S1: Figure 1) were selected for thorough cleaning and documentation. Four of them (A, B, C, and D) were located in the cross-section MP, whereas E and F were located in the SW cross-section (Figure 3b). This sampling procedure was intended to systematically record small, well-stratified areas. Profile D consisted of mixed materials and is not analyzed any further here. For each of the remaining five profiles, the macroscopic characteristics of each

stratigraphic unit (locus) were recorded, and artifacts were separately described and collected. For each locus, a sediment bulk sample (n = 41) was taken; radiocarbon samples (n = 9) were extracted whenever suitable material was available. The results of four C14 samples (Poz-131137; Poz-131180; Poz-131136; and Poz-130541; Table 3) were first published in Pollock et al. (2023).

To obtain an overview of the sedimentary architecture of the buried archaeological site beyond profiles A through F, the three brick pit cross-sections were cleaned and macroscopically documented. The position of potential cultural layers distinguishable macroscopically indicated additional sampling locations (n = 90). Cultural layers included features, such as presumable surfaces, ash layers, artifact concentrations, and even three sherds with largely complete profiles, potential trash areas, as well as alluvial pebble-sherd deposits.

In total, 131 sediment bulk samples were collected from Ajor Pazi (Supporting Information S1: Figure 1). Additionally, five samples were taken for luminescence dating at different positions in the SW cross-section, in what was assumed to be a sterile matrix surrounding the places that contain artifacts. The location of profiles A, B, C, E, and F, as well as macroscopic characteristics and the location of bulk samples for luminescence- and C14-dating within all three cross-sections, are displayed in Figure 3.

Profile C (MP cross-section) was selected as a key profile for in-depth sedimentological analysis. It is presented and discussed in detail.

2.2 | Sedimentological laboratory analysis

The 136 sedimentary bulk samples (131 + 5 residuals from luminescence samples) were analyzed for their chemical and physical characteristics at the Laboratory for Physical Geography, Department of Earth Sciences at Freie Universität. Sediment analyses included the measurements of carbon contents (TC, TOC), grain-size distribution, element composition, remissions, and magnetic susceptibility. Samples were prepared by crushing the aggregates, sieving (separating and discarding the fraction ≤/>2 mm Ø), and grinding an aliquot (~10 g) of the ≤2 mm Ø fraction with a vibrating agate disk mill.

2.2.1 | Remission

The remission values (CIE65 $L^*a^*b^*$) of each sample were measured on the sieved and air-dried material without specular component (SCE) using the CM-2500d portable spectrophotometer (Konica Minolta, Inc.) (Blum, 1997).

2.2.2 | Element composition

The element composition was determined using a portable energy dispersive X-ray fluorescence analyzer (pED-XRF) (Niton XLt3-900 GOLDD+; Thermo Fisher Scientific Inc.) on the ground and air-dried samples. Each sample was measured for 120 s using four filters in the in-device Cu/Zn "mining mode." Readings are calibrated internally and were output with 3.3-fold device internal error. Elements with a four-fold measurement error lower than the measured concentration were considered for further analyses (Ba, Nb, Zr, Sr, Rb, Pb, Zn, Fe, Mn, V, Ti, Ca, K, Si, and Al).

2.2.3 | Grain size

Grain size distributions (vol%) for fine fractions (≤ 2 mm Ø) were determined using a laser diffraction particle size analyzer (Beckmann-Coulter LS13 320). The samples were prepared by adding approximately 0.5 g of sodium pyrophosphate ($Na_4P_2O_7$) as an anti-coagulation agent. Due to geogenic carbonates that occur in the catchment of the Jajrud river and reported extensive secondary calcification, the inorganic carbon was not dissolved before the measurements (Schulte et al., 2016). Estimated grain-size distributions of each sample are based on the median of six measurements per sample. Particle sizes are categorized according to the German classification system of Ad-hoc-AG Boden (2005).

2.2.4 | Magnetic susceptibility

Volume-specific magnetic susceptibility (κ) at low (κlf; 0.465 kHz) and high (κhf; 4.65 kHz) frequencies were determined on air-dried and weighed samples using the MS2B sensor (Bartington Instruments). Each sample was measured five times in 12 cm³ containers at κlf and κhf and subsequently log-transformed, averaged, and inverse-transformed. The low-frequency mass-specific susceptibility (χlf) ($m^3 kg^{-1}$) and frequency-dependent susceptibility (χfd) (%) were calculated after Dearing (1999). Some samples could not be measured due to an insufficient amount of sample material (<12 cm³) and therefore are not represented within the overall sample population ($n = 123$).

2.2.5 | Carbon

The carbon contents (mass%) were determined by measuring total carbon (TC) and total organic carbon (TOC) and calculating total inorganic carbon (TIC) by subtracting TOC from TC. The TruSpec CHN (Leco) elemental analyzer was used to measure TC contents [mass-%] by dry combustion at 950°C and subsequent infrared spectroscopy. TOC content (mass%) was measured by catalytic oxidation at 680°C and subsequent NDIR detection using a TOC-L analyzer (Shimadzu) with 0.05 g of sample material. Before analysis, inorganic carbon was removed by adding 5 mL 1 N HCl. The manufacturer specifications of the TOC-L analyzer disclose a limit of detection of 0.025 $mg L^{-1}$ C and a limit of quantification of 0.089 $mg L^{-1}$ C according to DIN 32645 (Shimadzu, undated).

2.3 | Data analysis

2.3.1 | Multivariate statistics

Statistics were performed in Rstudio (v 4.1.0—R Core Team, 2013). The focus for the analysis of element compositions was on discriminating different intensities of weathering, soil formation, and grain-size effects. Due to the compositional restrictions of the element concentrations, biased measurement geometries, nonlinear absorption, and enhancement effects within the data matrix had to be considered (Tjallingii et al., 2007). Therefore, all element concentrations [ppm] considered (Ba, Nb, Zr, Sr, Rb, Pb, Zn, Fe, Mn, V, Ti, Ca, K, Si, and Al) were first separated from the overall composition and normalized to closure by converting them into an Aitchison composition ("acomp" in the R-package "compositions"; van den Boogaart & Tolosana-Delgado, 2008). Due to the small number of samples, we primarily address median values in our descriptions.

2.3.2 | Element ratios

Several commonly applied element ratios were calculated. To handle the compositional constraints and assess a robust statistical variation among the data, all element ratios were logarithmically transformed following the statistical theory of Aitchison (1982). Al/K ratio indicates chemical weathering due to the relative enrichment of Al weathering residues, while K gets removed easily due to its low ion potential (Buggle et al.,

2011). Rb/K is a commonly applied ratio connected to K-Feldspar weathering, which is understood as an intermediate level of chemical weathering (Buggle et al., 2011). The Ca/Sr ratio involves two explanatory approaches. Either Ca is leached much faster than Sr, thus forming a measure for decalcifying the sediment. Conversely, considering the in situ secondary calcification, the accumulation of carbonates can be addressed (Buggle et al., 2011; Profe et al., 2018); the latter is a more common feature for soils in arid to semi-arid regions of Iran (Khormali & Toomanian, 2018). Particularly regarding paleosurfaces, the Fe/Al ratio is an indicator of chemical weathering, as Fe is more effectively enriched under oxidizing conditions than Al (Feng, 1997). Concurrently, Fe enrichment can also be considered a hydromorphic feature that may lead to iron hydroxide precipitation in slack water (Barge et al., 2020). Additional ratios of Ti/Zr and Ti/Al were calculated as indications of grain-size sorting effects and, therefore, of the potential input of dust provenances (Profe et al., 2018).

2.3.3 | Principle component analysis (PCA)

Due to the size and the spatial dispersion of samples, the variability of the data was assessed by applying a PCA in Rstudio ("prcomp" in the R-package "stats"—R Core Team, 2013). For this purpose, the magnetic susceptibility data sets (χlf and χfd) could not be considered due to their noncontinuous measurements. The PCA is based on centered log-transformed TOC and TIC values ("clr" in the R-package "compositions"; van den Boogaart & Tolosana-Delgado, 2008) as well as the logarithmically transformed element ratios of Al/K, Rb/K, Ca/Sr, Fe/Al, Ti/Zr, and Ti/Al.

2.3.4 | Cluster analysis

Calculated principal components were evaluated in their contribution to the total explained variance using a scree plot and the Kaiser–Guttman criterion (Jolliffe, 2002). Scores of the selected principal components were distinguished by applying a cluster analysis based on parameterized finite Gaussian mixture models ("mclust" package in R—Scrucca et al., 2016). The derivation of the ideal number of clusters, as well as the model with the best approximation to the distribution of scores, have been selected using the Bayesian information criterion (BIC) ("fviz_mclust_bic" in the R-package "factoextra"—Kassambara & Mundt, 2020).

2.4 | Numerical dating

2.4.1 | Radiocarbon (C14)

Nine charcoal samples were dated at the Poznań Radiocarbon Laboratory in Poland. The resulting dates are calibrated using the OxCal software (v4.4.2—Bronk Ramsey, 1995). Atmospheric data are based on Reimer et al. (2020). Phenological classification of charcoal

remains was conducted in the archaeobotanical laboratory of the German Archaeological Institute by Dr. R. Neef and M. Dinies.

2.4.2 | Luminescence dating

Luminescence dating techniques, in general, allow the determination of depositional ages for sediments equivalent to the point in time when sediment grains were last exposed to daylight before subsequent deposition. Because of that, sample preparation was conducted at the VLL (Vienna Laboratory for Luminescence dating) under subdued red-light conditions following the preparation procedure described in Lüthgens et al. (2017) and Rades et al. (2018). All subsequent luminescence measurements using quartz and potassium-rich feldspar grains (150–250 μm) were conducted at the VLL on RISØ TL-OSL DA 20 automated luminescence reader systems (Bøtter-Jensen et al., 2000, 2003, 2010). Radionuclide determination was conducted at the VLL using high-resolution, low-level gamma spectrometry (Baltic Scientific Instruments [BSI] high purity Germanium [HPGe] p-type detector, ~52% efficiency) after samples were first dried and afterward stored in sealed Petri dishes (~60 g dry weight) for at least 1 month to establish secondary secular equilibrium.

First, tests showed that the luminescence signals of quartz were dim in general and lacked a dominant fast component necessary for dating. Because of that, dose recovery experiments were conducted using potassium-rich feldspar for selected samples. These showed recovery ratios in agreement with unity within error for both the IR50 and the pIRIR225 signals (infrared stimulated luminescence [IR] at 50°C and postinfrared infrared stimulated luminescence [pIRIR] at 225°C; Buylaert et al., 2009, 2012). Consequently, a pIRIR225 dating approach using 2 mm aliquots (each containing ~60 grains) was adopted for all subsequent measurements. Luminescence signals were stimulated using IR diodes and were detected through a LOT/Oriel D410/30 optical interference filter, selecting the K-feldspar emission at 410 nm (Krbetschek et al., 1997). Once corrected for fading (athermal signal loss over time; Wintle, 1973) using the approach of (e.g., Huntley & Lamothe, 2001), the resulting ages can be compared to detect incomplete bleaching in the samples (Buylaert et al., 2012; Murray et al., 2012). In the case of incomplete bleaching, a sample is expected to show increasing ages when comparing ages based on equivalent doses determined at lower temperatures (IR50) with those determined at higher temperatures (pIRIR225).

3 | RESULTS

3.1 | Sedimentological record

To provide an overview of the sedimentary architecture of the Ajor Pazi site, first, the macroscopic character of the three cross-sections is described, and sediment characteristics of the sampled loci are displayed. The focus is on profiles B, C, and F, with B and C located in

the MP cross-section opposite F in the SW cross-section (Figure 3). In addition to the detailed descriptions of these profiles, a summary of profiles A and E is provided in Supporting Information S4: Material 4 and Supporting Information S5: Figure 5). Stratigraphic units of the sediment profiles are delineated considering archaeological and sedimentological characteristics (e.g., artifacts, compaction, and pebble deposits) and, in general, comprise several layers/loci. For comparison of the sample allocation across all three cross-sections, depths refer to the excavated plane surface of Cut I (Figure 3b), which also corresponds to the excavated plane surface of the NE cross-section; all depths/heights are therefore noted as "above the ground surface" (a.g.s.). Instead of providing information on vertical sample allocation by "depth below surface," this modus operandi was chosen because, due to the strong human impact in the active quarrying site, surface topography underlies strong small-scale changes.

3.1.1 | Facies composition

Our sedimentological approach combines macroscopic descriptions retrieved during the archaeological rescue excavation with laboratory data. To link dispersed samples from the cross-sections with samples taken in the profiles, we reduced the dimensionality of our chemical and physical data sets by applying a PCA.

Following the Kaiser–Guttman rule (retain principal components (PC) with eigenvalues > 1.0), as well as a cumulative explained variance of the PCs > 80% (Jolliffe, 2002), the first four PCs are indicated as an optimal number (Table 1). PC 1 is primarily associated with the variation of TOC and TIC contents as well as Ca/Sr and Ti/Al ratios (Table 1). Characteristic of the second component is the variation of Ti/Al, Fe/Al, and Ti/Zr ratios (Table 1). PC 3 is mainly characterized by the variation of Ti/Zr, Fe/Al ratios, and partly by TIC values (Table 1). The ratio of Rb/K and TOC values represent the main contributors to PC 4 (Table 1).

As an additional reduction of dimensionality in our data, we examined the distribution of the resulting PCA scores through cluster analysis. The evaluation of the BIC resulted in the best possible description within two diagonal clusters of equal shape (VEI) (Supporting Information S2: Figure 2 and Supporting Information S3: Figure 3). Cluster I comprises the majority of samples ($n = 108$) and features a clayey silt texture with bi- to polymodal grain-size distributions; few samples in Cluster I contain fine to medium sands (Table 2; Supporting Information S8: Figure 8). The TOC concentration in Cluster I is relatively low, while TIC is enhanced; likewise, χlf values are low with high χfd levels (Table 2). It is evident that the element ratios of Al/K, Ca/Sr, as well as Ti/Zr, are high among the samples of Cluster I (Table 2). The second cluster includes 28 samples and is associated with a sandy texture that shows a bi- to polymodal grain size distribution (Table 2; Supporting Information S8: Figure 8). Samples of Cluster II are characterized by increased TOC and χlf values; the element ratios of Fe/Al, Rb/K, and Ti/Al are also higher than in Cluster I (Table 2).

Overall, the macroscopic properties, in combination with clusters of chemical and physical data, lead us to subdivide the sampled sediments of Ajor Pazi into three main facies types: (a) undifferentiated sediments without prominent stratification that are interspersed with (b) clearly layered, sandy and gravelly bands as well as (c) sediments characterized by increased TOC contents and χlf values (Table 2). Cluster I was not distinguished as independent facies, as we consider it to be a "base material" that is locally subdivided into facies "a" and "b" by its macroscopic characterization; Cluster II contains samples that are to be understood as deviations from the "base material." In addition to the three main facies types, scattered wall-like structures were identified during the excavation of the SW and MP cross-sections, primarily composed of very compacted clayey silt. Moreover, the SW cross-section contained a highly concentrated burnt clay and sherd layer that was classified separately (Figure 3).

Due to the lack of distinct stratification, *facies "a"* was punctually sampled ($n = 48$) across the cross sections; samples are rather

TABLE 1 Eigenvalues of the principal components (PC) derived from the chemical sediment data set and distribution of the explained variance among the principal components.

PC	Eigenvalue	EV [%]	CEV [%]	Contribution [%]							
				TOC	TIC	AL/K	Ca/Sr	Fe/Al	Rb/K	Ti/Zr	Ti/Al
1	2.70	33.73	33.73	25.26	22.22	14.33	23.43	0.65	9.17	3.98	0.95
2	2.03	25.37	59.10	0.73	1.43	8.83	1.15	23.12	1.85	20.51	42.37
3	1.19	14.86	73.96	3.67	18.46	3.25	6.39	32.39	2.70	33.06	0.07
4	1.00	12.51	86.47	14.35	11.52	11.91	0.05	5.95	54.06	0.15	2.01
5	0.48	6.01	92.47	7.43	2.18	52.02	0.33	4.44	27.71	1.28	4.62
6	0.40	5.05	97.53	15.12	0.12	5.91	65.41	1.48	1.79	9.31	0.86
7	0.14	1.76	99.29	0.40	0.50	0.34	0.00	27.55	0.18	23.71	47.31
8	0.06	0.71	100.00	33.04	43.56	3.41	3.24	4.41	2.55	7.99	1.80

Note: The optimal number of principal components is displayed by the gray-dotted line.

Abbreviations: CEV, cumulative explained variance; EV, explained variance; PC, principal component.

TABLE 2 Statistical overview of the sedimentological parameters characterizing clusters I and II, complemented by the statistical overview of the sedimentological parameters characterizing facies "a" and "b".

	Statistical Parameter	[vol-%]			L*	a*	b*	[mass. %]		χlf	χfd	Ln (Al/K)	Ln (Ca/Sr)	Ln (Fe/Al)	Ln (Rb/K)	Ln (Ti/Zr)	Ln (Ti/Al)
		Clay	Silt	Sand				TOC	TIC								
Cluster I																	
	Min.	3	13	0	47	4	15	0.05	1.20	27	0.08	0.88	4.64	−0.98	−5.75	2.52	−3.02
	Max.	28	90	83	68	7	19	0.97	3.56	206	7.57	1.18	5.62	−0.64	−5.51	3.48	−2.77
	μ	13	64	23	56	6	17	0.24	2.46	97	3.00	1.02	5.23	−0.80	−5.62	3.13	−2.90
	σ	6	24	29	5	1	1	0.15	0.44	36	1.72	0.06	0.25	0.07	0.05	0.15	0.06
	CV [%]	46	38	126	9	17	6	63	18	37	57	6	5	9	1	5	2
	Median	13	79	3	55	6	16	0.20	2.51	91	2.67	1.01	5.31	−0.80	−5.62	3.16	−2.90
	MAD	7	11	5	5	1	1	0.10	0.40	34	1.66	0.06	0.20	0.07	0.04	0.15	0.06
	COV [%]	54	14	167	9	17	6	50	16	37	62	6	4	9	1	5	2
Cluster II/Facies "c"																	
	Min.	1	4	0	44	3	12	0.03	0.26	51	0.65	0.76	3.58	−1.11	−5.95	2.28	−3.18
	Max.	19	86	94	62	8	20	2.67	3.56	427	7.47	1.23	5.71	−0.56	−5.49	3.58	−2.56
	μ	7	42	51	51	5	15	0.41	2.12	170	3.48	0.96	5.03	−0.73	−5.68	2.99	−2.82
	σ	5	28	33	5	1	2	0.54	0.84	96	2.67	0.11	0.50	0.13	0.10	0.34	0.15
	CV [%]	71	67	65	10	20	13	132	40	56	77	11	10	18	2	11	5
	Median	6	40	53	50	5	16	0.20	2.00	155	2.06	0.95	5.21	−0.74	−5.67	2.93	−2.84
	MAD	3	36	38	4	1	2	0.14	0.85	77	2.09	0.07	0.34	0.13	0.07	0.43	0.13
	COV [%]	50	90	72	8	20	13	70	43	50	101	7	7	18	1	15	5
Facies "a"																	
	Min.	4	15	0	49	5	15	0.07	1.50	27	0.08	0.88	4.73	−0.90	−5.72	2.52	−3.01
	Max.	28	87	81	68	7	19	0.53	3.56	153	6.16	1.18	5.48	−0.64	−5.51	3.48	−2.77
	μ	15	74	10	58	6	17	0.24	2.57	81	2.83	1.01	5.24	−0.77	−5.61	3.16	−2.90
	σ	5	17	21	4	1	1	0.10	0.35	30	1.40	0.07	0.20	0.07	0.04	0.16	0.06
	CV [%]	33	23	210	7	17	6	42	14	37	49	7	4	9	1	5	2
	Median	17	81	0	59	6	17	0.21	2.58	72	2.67	1.01	5.31	−0.78	−5.62	3.20	−2.90
	MAD	4	3	0	5	0	1	0.06	0.31	25	1.25	0.07	0.15	0.07	0.04	0.07	0.08
	COV [%]	24	4	NaN	8	0	6	29	12	35	47	7	3	9	1	2	3
Facies "b"																	
	Min.	3	13	0	47	4	15	0.05	1.20	43	0.56	0.89	4.64	−0.98	−5.75	2.74	−3.02
	Max.	19	90	83	65	6	18	0.97	3.40	206	7.57	1.12	5.62	−0.67	−5.53	3.38	−2.79
	μ	9	50	41	53	5	16	0.25	2.32	113	3.04	1.01	5.23	−0.82	−5.63	3.09	−2.89
	σ	5	26	30	4	0	1	0.19	0.51	37	2.09	0.05	0.30	0.07	0.05	0.15	0.06
	CV [%]	56	52	73	8	0	6	76	22	33	69	5	6	9	1	5	2
	Median	9	52	39	53	5	16	0.19	2.25	103	2.53	1.01	5.34	−0.83	−5.63	3.07	−2.89
	MAD	5	41	47	4	0	1	0.11	0.55	31	2.06	0.06	0.29	0.07	0.06	0.17	0.06
	COV [%]	56	79	121	8	0	6	58	24	30	81	6	5	8	1	6	2
Wall−like structures																	
	Min.	8	59	0	54	5	16	0.08	2.03	67	1.41	1.00	4.91	−0.88	−5.64	3.03	−3.00
	Max.	20	88	33	57	7	18	0.56	2.84	144	5.88	1.15	5.43	−0.76	−5.53	3.27	−2.83

TABLE 2 (Continued)

Statistical Parameter	[vol-%] Clay	Silt	Sand	L*	a*	b*	[mass. %] TOC	TIC	χlf	χfd	Ln (Al/K)	Ln (Ca/Sr)	Ln (Fe/Al)	Ln (Rb/K)	Ln (Ti/Zr)	Ln (Ti/Al)
μ	15	81	4	55	6	17	0.21	2.56	99	3.58	1.06	5.19	−0.80	−5.59	3.15	−2.92
σ	3	8	9	1	0	1	0.14	0.23	27	1.33	0.05	0.19	0.03	0.03	0.07	0.05
CV [%]	20	10	225	2	0	6	67	9	27	37	5	4	4	1	2	2
Median	15	84	0	55	6	17	0.16	2.61	90	3.57	1.04	5.25	−0.80	−5.60	3.16	−2.92
MAD	2	4	0	0	0	1	0.12	0.22	22	1.07	0.03	0.17	0.02	0.04	0.08	0.05
COV [%]	13	5	NaN	0	0	6	75	8	24	30	3	3	3	1	3	2

Note: Samples of Cluster I were subdivided into the macroscopically described facies "a" and "b." Samples in Cluster II correspond to facies "c." Samples taken from archaeologically identified "wall-like structures" were not assigned to any facies.

Abbreviations: COV, median-centered coefficient of variation; CV, coefficient of variation; MAD, median absolute deviation.

heterogenous and show a highly variable texture, ranging between clayey to sandy-loamy silt and silty sand (Table 2). The comparatively high TIC concentrations are the sole distinctive feature of this facies (Table 2).

The bands of *facies "b"* traverse all cross-sections and emerge predominantly in the vertically lower to central parts of the sections (0–3 m a.g.s.; Figure 3). Grain sizes <2 mm Ø of the samples among facies "b" have coarser textures than in facies "a" and "c" but vary between cross-sections (Table 2). Additionally, the fines (<2 mm fraction) sampled from the pebble layers show a slightly higher magnetic susceptibility (χlf) than the over and underlying sediments.

Facies "c" (*n* = 28) comprises samples with features, such as distinctively increased TOC concentrations, high χlf values as well as increased element ratios displaying weathering activity (Fe/Al, Rb/K; Table 2).

It is possible to distinguish between facies "a" and "b" macroscopically based on their stratification; sediments of facies "c" would fit into the first two facies macroscopically but can be distinguished by their chemical and physical characteristics. The spatial distribution of the laboratory data-based clusters shows distinct accumulations in the SW cross-section and partially in the NE section; samples collected from the MP cross-section are poorly described by facies "c."

3.1.2 | Cross-sections

The NE cross-section strikes NW and is exposed to the NE; it is approximately 50 m long (Figure 3). Nineteen loci were identified, of which 18 were sampled. Facies "a" characterizes the NE cross-section, traversed by up to 40-cm-thick bands of sandy and gravelly layers, locally associated with facies "b." The sandy layers of facies "b" primarily overlay the pebble layers. Sediments of facies "c" were identified in 6 out of 18 samples, most of them were embedded in layers of facies "b."

The *SW cross-section* is approximately 61 m long and comprises the profiles E and F (Figure 3). The section strikes NW and is exposed

to the SW. Forty bulk samples were analyzed, five of which are from within profile F. Profile E was macroscopically described but not sampled. Material of facies "a" characterizes the SW cross-section, traversed by up to 40-cm-thick bands of sandy and gravelly layers, locally associated with facies "b." Prominent in facies "b" was a cavity at the E profile level; the cavity's remains were composed of sand and pebbles. Sediments of facies "c" were identified in 14 out of 40 samples, most of them were embedded in layers of facies "b." The SW cross-section contains four scattered wall-like structures as well as one layer described macroscopically as consisting of burnt clay and sherds at the bottom of the section (Figure 3).

The analyzed *MP cross-section* (Main Profile) is approximately 54 m long and encompasses the profiles A, B, and C (Figure 3). The section strikes NW and is exposed to the NE. A total of 78 bulk samples were extracted, of which 10 were extracted from profile A, six from profile B, and 20 from key profile C. The MP section is characterized primarily by sediments associated with facies "a," which were traversed by several sandy and gravelly bands of facies "b." Across the MP section, sandy bands in facies "b" are thicker (30–40 cm) than the pebble layers (5–10 cm). Eight out of the 78 samples of the MP cross-section fit into Cluster II and were therefore associated with facies "c." Ten isolated wall-like structures were identified within the MP cross-section; it appeared that bands of facies "b" partly connected these structures. Next to key-profile C, the profile B (Supporting Information S6: Figure 6) was described in detail.

3.1.3 | Key-profile C

Key-profile C, with a vertical extent of 311 cm, is located approximately 5 m northwest of profile B within the MP cross-section. The top of the profile is located 47 cm beneath the surface of the MP cross-section and 300 cm above the ground surface of Cut I (Figure 3). Twenty-one loci are located in nine stratigraphic units; 20 of the loci were sampled. The key-profile features predominantly silty material with thin gravel inclusions in the stratigraphic Units VI and

VII and a relatively high quantity of archaeological material between the lower ends of Units I and VII.

1. The uppermost Unit I is 115 cm thick (300–185 cm a.g.s.) and divided into five loci (2, 3, 4, 5, and 6) with similar colorations but alternating clayey silt to sandy silt texture. The top Loci 2 (300–272 cm a.g.s.) and 3 (272–254 cm a.g.s.) show a similar brownish color and are composed of clayey silt. Loci 4 (263–216 cm a.g.s.) and 5 (240–210 cm a.g.s.) have a similar brownish color to the overlying samples but a sandy silt texture, with locus 4 firmly compacted. The bottom Locus 6 (210–177 cm a.g.s.) has a similar brownish coloration as the other loci of the unit and consists of clayey silt. Both lower loci (5 and 6) contain bone fragments and sherds.

2. Unit II (202–177 cm a.g.s.) covers the right profile side next to Locus 6 and comprises Locus 7, which is of a darker brownish color than the overlying loci of Unit I. Sediments of Locus 7 show a sandy-loamy silt texture, are firmly compacted, and do not feature any archaeological material.

3. Unit III (177–168 cm a.g.s.) consists exclusively of Locus 8, with a brownish color slightly darker than those in Unit I but lighter than in Unit II. Locus 8 is of clayey silt texture with a low sand content and is firmly compacted. A few charcoal pieces occurred within Locus 8.

4. Unit IV includes Loci 9, 10, and 11, with an overall thickness of 46 cm (168–122 cm a.g.s.). It consisted entirely of clayey silt and was distinguished by the presence of archaeological features. Locus 9 (177–153 cm a.g.s.), on the left side bounded by Locus 8 of Unit III, was of a light brownish color, while Locus 10 (168–131 cm a.g.s.) is reddish brown. Locus 11 (147–122 cm a.g.s.) was light brown but brighter than Locus 9. Loci 11 and 10 contain pottery sherds, with bone fragments additionally identified in Locus 10.

5. Unit V (128–120 cm a.g.s.) consists exclusively of Locus 21. Its prominent feature is the dark grayish color of the clayey silt material.

6. Unit VI (124–87 cm a.g.s.) encompasses five loci (12, 13, 14, 15, and 17) that hardly differed in their light brownish color and a slight dip to the southeast. The loci of Unit VI featured an alternating texture, with coarse components in Loci 12 and 14. Locus 12 (124–118 cm a.g.s.) is the darkest brown one in Unit VI, with a clayey-sandy silt texture. Locus 13 (122–96 cm a.g.s.) featured a light brownish color and was characterized by clayey silt that was hardly compacted. C14 dating of a charcoal sample from Locus 13 yields an age of 6296–6002 cal. B.P. (4346–4052 cal. B.C.E.; 2σ). The underlying Locus 14 (114–92 cm a.g.s.) shows the lightest brownish coloration in Unit VI and is composed of clayey silt with a small amount of fine, well-rounded gravel.

The uppermost locus (12) of Unit VI included traces of burnt clay. Loci 13 and 14 featured sherds and charcoal, with the addition of bone fragments in Locus 13. Locus 15 contained charcoal, sherds,

bones, and burnt clay pieces. Charcoal fragments were identified in Locus 17. An age of 6280–6003 cal. B.P. (4330–4053 cal. B.P.; 2σ) was obtained from radiocarbon dating of a charcoal sample from Locus 17.

1. Unit VII (92–81 cm a.g.s.) consists of Locus 16, which displays a light brownish color and marks the lower end of the sloping layers in Unit VI. The texture of Locus 16 is clayey silt and contains a large amount of partially rounded fine gravel (2–5 cm).

2. Unit VIII (92–1 cm a.g.s.) is comprised of Loci 20, 19, and 18, which are all composed of a clayey silt texture. Locus 18 (91–40 cm a.g.s.) is divided into a right and left part by Locus 19; both sides display a reddish-brown color (Figure 4). Locus 19 (91–42 cm a.g.s.) has the same light brownish coloration as the underlying Locus 20 (42–1 cm a.g.s.). In Locus 19 roots occur.

3. The basal Unit IX (1–(−11) cm a.g.s.) corresponds to Locus 22 (unsampled), which displays a light brownish color and is highly compacted.

The key-profile C shows low variations among all parameters (Figure 4). TOC and TIC concentrations run parallel throughout the profile in a low to moderate range but are markedly higher in Unit 2, Locus 7 (Figure 4). This deviation of Locus 7 is evident in almost all parameters. The brightness (L^*) of Locus 7, as well as of the underlying locus 8, is distinctly lower than the rest of the samples. The χlf and χfd values indicate that in addition to Locus 7, Loci 12 and 17 (Unit VI) deviate from the surrounding samples. The deviation of Locus 12 within the range of χlf and χfd values is less pronounced than in Locus 17; correspondingly, the log-transformed ratios of Al/K and Fe/Al show a distinctly lower value for Locus 12 than for the surrounding samples. In addition, Loci 7 and 12 are the only loci that were assigned to the second cluster. The ratio of Ca/Sr shows low variations across the profile, with the lowest values in Loci 4 and 5 (Unit I) and Locus 7 (Unit II). The variations among the other ratios calculated do not show distinct deviations (Figure 4).

3.1.4 | Profiles B and F

Profile B (Supporting Information S6: Figure 6) was part of the MP cross-section, located approximately 5 m SE of profile C (Figure 3). It vertically extended 220 cm, and the top of the profile is located 147 cm beneath the surface of the MP cross-section. Nine loci were identified that included five stratigraphic units; six of the loci were sampled. The profile featured wall-like consolidated material on top of a disturbed sequence of sandy material with enclosed fine sediments toward the lower end of the profile.

1. The uppermost Unit I (216–121 cm a.g.s.) comprises Loci 4, 3, and 2, of which Loci 4 and 2 (216–149 cm a.g.s.; unsampled) run parallel and consist of light brown wall-like consolidations. Locus 3 (149–121 cm a.g.s.) had a grayish-brown, sandy-loamy silt texture and was highly compacted. In addition to sherds, charcoal, and
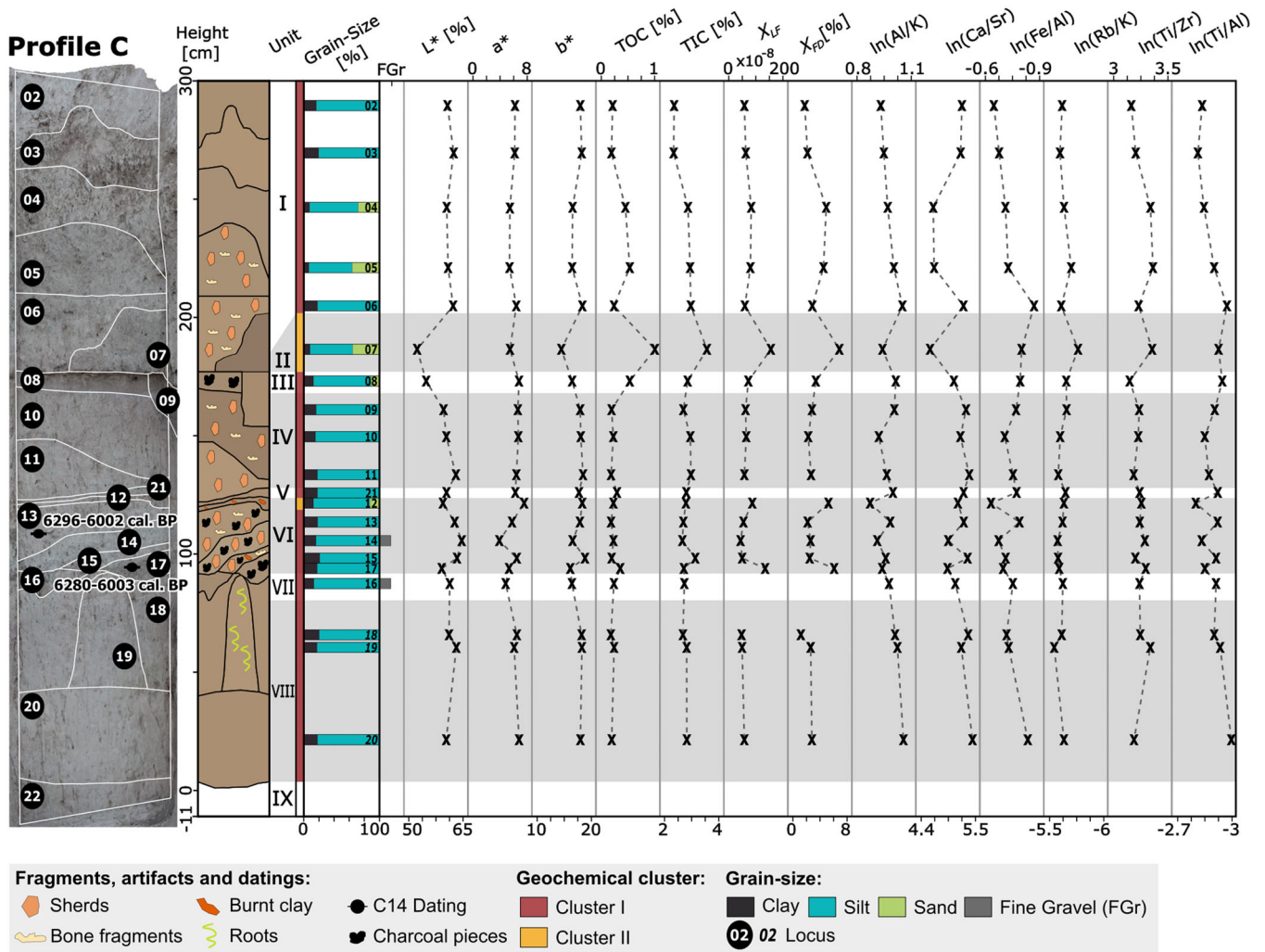
FIGURE 4 Macroscopic description, bulk chemistry, and elemental composition of key profile C. Heights are related to the surface level of "Cut I" (Figure 3) to approximate similar levels between all three key profiles. Grain size classification based on Ad-hoc-AG Boden (2005). Calibrated radiocarbon ages are given at the 95% confidence level (Table 3). The colors of the layers are based on the remission values measured under laboratory conditions.

roots occurred in Locus 3. Radiocarbon dating of a charcoal sample from Locus 3 yielded an age of 6302–6020 cal. B.P. (4352–4070 cal. B.P.; 2σ).

2. Unit II (121–27 cm a.g.s.) encompasses Loci 5 and 6, with Locus 5 being further subdivided. The overall matrix of Locus 5 was sandy silt and included traces of charcoal, sherds, and bone fragments. C14 dating of a sample of charcoal from Locus 5 yields an age of 6395–6210 cal. B.P. (4445–4260 cal. B.C.E.; 2σ). The underlying Locus 6 (37–27 cm a.g.s.) was composed of light brownish silty sand. Both loci of the second unit belong to the second geochemical cluster. Overall, the sand content increases from top to bottom. Locus 5 (121–37 cm a.g.s.) is characterized by stains of different colors; the base matrix (121–65 cm a.g.s.) is dark brown. At different levels on the left (75–60 cm a.g.s.) and right side of the profile (113–94 cm a.g.s.), two dark gray compacted inclusions, including pieces of burnt clay, occur in Locus 5. Between 84 –and 43 cm a.g.s. the sediment color changes to reddish brown with a single bone fragment embedded.

The lowest section of Locus 5 (49–37 cm a.g.s.) corresponds to a greenish to light gray ash. In the central part (94–75 cm a.g.s.) of Locus 5, angular clasts (3–5 cm) occur.

3. Unit III (30–27 cm a.g.s.) corresponds to the reddish-brown Locus 7 and is composed of slightly compacted clayey silt.

4. Unit IV (−4 to 27 cm a.g.s.) comprises Loci 8 and 10, composed of a clayey silt texture. Locus 8 (27–3 cm a.g.s.) has a light brown color, while the underlying Locus 10 (3 to −4 cm a.g.s.) is slightly darker. Locus 10 is distinguished from Locus 8 because it contains burnt clay and charcoal.

5. Unit V corresponds to Locus 11 (−4 to (−31) cm a.g.s.), which shows a light brownish coloration and is macroscopically described as compacted sandy material with a single sherd and a single bone in the upper part.

The limited number of samples prevents a reliable identification of trends in Profile B. TOC concentrations of the samples show an inverse pattern to L* values and reach maximum concentrations in

Unit II, Locus 5. The TIC concentrations are largely constant without distinct trends. χlf and χfd values follow a parallel trend, with high values in Units I to II. Almost all parameters show lower values between Locus 6 (Unit II) and the underlying Locus 7 (Unit III) (Supporting Information S6: Figure 6).

Profile F is located at the SE end of the SW cross-section and faces key-profile C at the opposite side of "Cut I" (Figure 3). The profile begins at the top of the SW cross-section and is 259 cm high (supplementary material Figure 7). Fifteen loci were assigned to 11 stratigraphic units; five of the loci were sampled. The profile features alternating sandy to silty textures with a compacted layer on top of gravel and a thinner ashy layer.

1. Unit I (242–214 cm a.g.s.) corresponds to Locus 2. The unit is characterized by a light brown color and coarse unsorted material with larger clasts (5–10 cm).

2. Unit II (233–125 cm a.g.s.) encompasses macroscopically described Loci 3, 4, and 5. Locus 3 (233–166 cm a.g.s.) has a light brown color with a compacted silty sand texture. Locus 4 (199–168 cm a.g.s.) is a sandy intrusion formed on the right side of Locus 3 and shows the same light brown color as Locus 3. Locus 5 (166–125 cm a.g.s.) has a reddish-brown color and shows a silty sand texture as in Locus 3, but also contains scattered angular clasts (2–5 cm).

3. Unit III (141–111 cm a.g.s.) corresponds to Loci 6 and 7, which both show an angled layering, sloping toward the right side of the profile. Locus 6 (141–115 cm a.g.s.) is dark brown with a clayey-sandy silt texture. Locus 7 (121–111 cm a.g.s.) shows a slightly darker brownish color with a similar clayey-sandy silt texture. Both loci contain archaeological finds: a relatively large amount of pottery and burnt clay pieces, bone fragments, and charcoal.

4. Units IV, V, and VI correspond to the macroscopically described Loci 9, 10, and 11. Locus 9 (111–96 cm a.g.s.) displays a light brown coloration composed of very fine sorted material firmly compacted. Locus 10 (96–83 cm a.g.s.) has a light grayish-brown color and is compact. Locus 11 (101–67 cm a.g.s.) shows a light brownish color and is porous with a weakly compacted structure and poor sorting.

5. Unit VII (82–42 cm a.g.s.) comprises Loci 12 and 14, with Locus 14 being a dark grayish inclusion within Locus 12. Locus 12 (82–42 cm a.g.s.) displays a brown color composed of a clayey silt texture, while Locus 14 (62–57 cm a.g.s.) is characterized by sandy silt. Scattered burnt clay pieces and charcoal remnants were noted for Locus 12. C14 dating from Locus 12 indicates an age between 6441 and 6292 cal. B.P. (4491–4342 cal. B.C.E.; 2σ) (Pollock et al., 2023).

6. Units VIII, IX, and X correspond to the macroscopically described Loci 16, 17, and 18. Locus 16 (50–42 cm a.g.s.), a light brown layer, was composed of poorly sorted medium to coarse sand. Locus 17 (47–28 cm a.g.s.) is firmly compacted. Locus 18 (37–26 cm a.g.s.) has a grayish coloration that contains scattered pebbles. C14 dating of charcoal in Locus 16 yielded an age between 6437 and 6191 cal. B.P. (4487–4241 cal. B.C.E.; 2σ) (Pollock et al., 2023).

7. The basal Unit XI (26 to −17) cm a.g.s.) is comprised of Locus 19 with a dark brownish color and a sandy-loamy silt texture. High

numbers of bones, burnt clay, and charcoal pieces were identified. The latter could be dated to an age of 6389–6128 cal. B.P. (4439–4178 cal. B.C.E.; 2σ) (Pollock et al., 2023).

The limited number of samples prevents the identification of distinct trends in Profile F. The graph of TOC concentrations runs inversely to the sediment albedo, as displayed in the L* values. The TIC is constant at a medium level throughout the sampled units. χlf and χfd follow a synchronous pattern, where values are high in Unit III, diverging between a low (Locus 12) and medium (Locus 14) level in Unit VII and high again in Unit XI. Apart from the Ti/Al ratio, the most prominent pattern within all element ratios is the strong divergence of Loci 12 and 14 in Unit VII.

3.2 | Numerical dating

3.2.1 | Radiocarbon dating

Radiocarbon dating (Table 3) yielded results showing a very low temporal variability. Eight out of the nine radiocarbon-dated samples are dated between 6441 and 6002 cal. B.P. (second half of the fifth millennium B.C.E.); only the sample from profile A is slightly younger and dates to 5904–5605 cal. B.P., or 3954–3655 cal. B.C.E. (2σ).

3.2.2 | Luminescence dating

Five samples from the SW cross-section were dated using IR50 and pIRIR225 luminescence signals for the dating of feldspar (Table 4). Based on the rejection criteria derived from dose recovery experiments (recycling ratio/recuperation in % of the natural signal/maximum test dose error = 20/20/20%), the resulting equivalent dose distributions were generally normally distributed, only including a few higher outliers for both signals. Because of that, average equivalent doses were calculated using the central age model (CAM) of Galbraith et al. (1999). Overall, dose rate and age calculation were conducted using ADELE software (Table 4; Kulig, 2005). Details on the radionuclide content and the overall dose rate calculations are provided in Table 4. Fading experiments following the approach of Auclair et al. (2003), but adapted to include the pIRIR225 signal, showed average g-values of 4.0 ± 0.9 for the IR50 signal and 1.5 ± 0.5 for the pIRIR225 signal. These average values were used for fading correction of all samples following the approach of Huntley and Lamothe (2001), calculated using the R-luminescence package (Kreutzer et al., 2012) (Table 4). Comparing the pairs of IR50 and pIRIR225-based ages for all samples, both ages are in good agreement within error for all individual samples, which provides a strong argument that incomplete bleaching was not significant in the depositional process. Therefore, no significant age overestimation occurs. However, as the IR50 signal is better bleachable in nature, the IR50-based ages are used for all subsequent interpretations. All

TABLE 3 Results from radiocarbon dating of the sediment samples from Ajor Pazi.

Profile	Depth [cm a.g.s]	Profile/ locus	Lab-code	C14 age	Calibrated Age [B.C.E.]	Calibrated Age [B.P.]	Confidence [%]	Botanical classification	Facies
A	120	A/11	Poz-149338	5020 ± 60	3954–3701	5904–5651	89.4	-	
					3684–3655	5634–5605	6.0		
B	135	B/03	Poz-148843	5420 ± 40	4352–4228	6302–6178	86.2	Deciduous wood	b
					4196–4167	6146–6117	6.8		
					4094–4070	6044–6020	2.4		
	79	B/05[a]	Poz-131137	5500 ± 35	4445–416	6395–6366	14.2	Deciduous wood	c
					4406–4322	6356–6272	67.3		
					4292–4260	6242–6210	13.9		
	15	B/08	Poz-130541	5460 ± 40	4439–4426	6389–6376	1.5	Deciduous wood	a
					4365–4240	6315–6190	93.3		
					4185–4178	6135–6128	0.7		
C	109	C/13	Poz-149476	5390 ± 60	4346–4156	6296–6106	73.4	Deciduous wood	c
					4140–4052	6090–6002	22.0		
	94	C/17	Poz-150113	5360 ± 40	4330–4280	6280–6230	18.8	Deciduous wood	a
					4275–4157	6225–6107	46.7		
					4139–4053	6089–6003	29.9		
F	62	F/12[a]	Poz-131180	5570 ± 40	4491–4473	6441–6423	3.8	Deciduous wood - *Rhamnus*	a
					4460–4342	6410–6292	91.6		
	46	F/16[a]	Poz-131136	5500 ± 60	4487–4479	6437–6429	0.6	-	-
					4457–4241	6407–6191	94.8		
	4	F/19[a]	Poz-130541	5460 ± 40	4439–4426	6389–6376	1.5	Deciduous wood	b
					4365–4240	6315–6190	93.3		
					4185–4178	6135–6128	0.7		

[a]Published in Pollock et al. (2023).

samples show good agreement within error and with independent age control from radiocarbon dating.

Four out of five samples date between 8.7 ± 1.3–7.1 ± 1.1 ka B.P. (Table 4). Only the OSL-7-APZ sample represents a low outlier (4.3 ± 0.6 ka B.P.); neither the dosimetry (dose rate determination) nor the luminescence-related (equivalent dose determination, fading) results show any irregularities compared to the rest of the data set. Since an introduction of younger grains into the sediment also seems unlikely based on the sedimentology of the section under investigation, the reason for the occurrence of the outlier remains unclear.

4 | DISCUSSION

4.1 | Chronology

To understand the past morphodynamics at Ajor Pazi, it is fundamental to situate the site in its temporal framework. Numerical

dating methods (C14: 6441–5605 cal. B.P./ca. 4490–3655 cal. B.C.E.; Luminescence dating: 8.7 ± 1.3–4.3 ± 0.6 ka B.P.; Tables 3 and 4) as well as the relative dating of archaeological finds, primarily pottery, point to occupational periods and morphodynamics consistently with a time range between 9 and 4 ka B.P. Considering the uncertainty of the luminescence ages, the sedimentary base upon which Ajor Pazi was deposited dates approximately into a time range between 8 and 7 ka B.P. Despite its low uncertainty, the result of the youngest dating (OSL-7-APZ) is considered an outlier due to its close location between samples OSL-5-APZ and OSL-6-APZ, which show overlapping ages within the error (Table 4).

Regarding the C14 ages of charcoal remains, it has to be considered that the sediments they were embedded in were due to the alluvial setting repeatedly redeposited and reworked before deposition at the Ajor Pazi site. All C14 samples were collected from deposits with an archaeological context. Stratigraphically, these were introduced after the fan material was deposited, and thus the radiocarbon ages tend to be younger than the OSL-dated sediments.

TABLE 4 Results from radionuclide analysis and luminescence dating of sediment samples from Ajor Pazi.

Lab code	Field code	238U (Bq/kg)	232Th (Bq/kg)	40K (Bq/kg)	Depth (m)	(cm a.g.s)	Overall dose rate Fs (Gy/ka)[a]	IR50 (n)[b]	pIRIR 225 (n)[b]	IR50 D_e (Gy)[b]	pIRIR225 D_e (Gy)[c]	IR50 (ka) faded[d]	IR50 (ka) fading corr.[d]	pIRIR225 (ka) faded[d]	pIRIR225 (ka) fading corr.[e]
VLL-0501-L	OSL-3-APZ	28.76 ± 2.04	27.88 ± 1.93	145 ± 23	1.69	245	2.31 ± 0.21	29	19	11.64 ± 0.58	15.51 ± 1.14	5.1 ± 0.5	7.4 ± 1.2	6.7 ± 0.8	7.7 ± 0.9
VLL-0502-L	OSL-4-APZ	24.18 ± 1.83	21.34 ± 1.49	343 ± 21	2.37	179	2.69 ± 0.20	14	8	15.93 ± 1.29	23.36 ± 1.88	5.9 ± 0.7	8.7 ± 1.3	8.7 ± 1.0	9.8 ± 1.1
VLL-0503-L	OSL-5-APZ	27.35 ± 2.06	23.41 ± 1.91	429 ± 26	3.54	52	3.00 ± 0.23	19	16	14.61 ± 1.03	23.32 ± 1.44	4.7 ± 0.5	7.2 ± 1.3	7.8 ± 0.8	8.7 ± 1.0
VLL-0504-L	OSL-6-APZ	24.57 ± 2.09	22.24 ± 1.56	535 ± 32	2.28	178	3.26 ± 0.25	17	11	15.34 ± 1.31	21.23 ± 1.40	4.7 ± 0.5	7.1 ± 1.1	6.5 ± 0.7	8.8 ± 0.9
VLL-0505-L	OSL-7-APZ	23.60 ± 2.01	27.61 ± 1.82	343 ± 21	3.11	98	2.73 ± 0.20	24	20	8.00 ± 0.70	12.16 ± 1.06	3.0 ± 0.3	4.3 ± 0.6	4.5 ± 0.5	5.1 ± 0.7

[a]Cosmic dose rate determined according to Prescott and Stephan (1982) and Prescott and Hutton (1994), taking the geographical position of the sampling spot (longitude, latitude, and altitude), the depth below the surface, as well as the average density of the sediment overburden into account. An uncertainty of 10% was assigned to the calculated cosmic dose rate. External and internal dose rates were calculated using the conversion factors of Adamiec and Aitken (1998) and the β-attenuation factors of Mejdahl (1979), including an alpha attenuation factor of 0.08 ± 0.01 and an internal K content of 12.5 ± 0.5% (Huntley & Baril, 1997) and estimated average water content of 8 ± 4% (VLL-0502/0503/0504-L) and 10 ± 4% (VLL-0501/0505-L) throughout burial time, respectively. The error was propagated to the overall dose rate calculation.

[b]Number of aliquots passing all rejection criteria.

[c]Calculated using the CAM (Central Age Model, Galbraith et al. 1999).

[d]Calculated using the software ADELE (Kulig, 2005).

[e]Corrected for fading according to the method of Huntley and Lamothe (2001) using the R Luminescence package (Kreutzer et al., 2012).

Although the narrow scatter of ages argues for a relatively consistent chronology, we address the C14 dates as maximum depositional ages given the alluvial setting (Chiverrell et al., 2011). These dates and the associated archaeological finds allow a narrowing of the first period of occupation at Ajor Pazi to a time between ca. 6441 and 6002 cal. B.P. (ca. 4491–4052 cal. B.C.E., archaeologically, the Transitional Chalcolithic II). The dating from Locus 11 of the A profile (5904–5605 cal. B.P./3954–3655 cal. B.C.E.; Table 3) is an expected outlier: profile A was laid out at the location of a largely complete vessel identifiable as dating to the Late Chalcolithic period. This was already visible at the start of work at Ajor Pazi in the walls of the MP cross-section about 25 m SE of the key-profile C. Considering the numerical dating results, the presumable period of fluvial dynamics displayed in the sediment outcrop at Ajor Pazi dates to about 8–5.6 ka B.P.

The archaeological material from Ajor Pazi that was sampled in 2018 corresponds to the poorly documented Transitional Chalcolithic II. Pollard et al. (2013) suggested the TC II period to fill the undated gap in the long-term regional 14C sequence, which lasted from 6550–6250 B.P. to 4600–4300 B.C.E. (Pollard et al., 2013). The TC II period postdates the latest radiocarbon dates from the site of Cheshmeh Ali in the adjacent Tehran plain (Fazeli et al., 2004) and falls into the time of the temporary abandonment of Tappeh Pardis, a Neolithic to Transitional Chalcolithic I site in the Varamin Plain, around 6650 B.P. (Fazeli et al., 2007). However, it predates the Early/Middle Chalcolithic occupation in the plain, as the recently excavated material and radiocarbon dates from the settlements of Chaltasian and Ahmadabad-e Kuzehgaran, respectively, 8 and 15 km to the northwest of Ajor Pazi (Pollock et al., 2023). As reported from the archaeological sites of Tappeh Pardis and Cheshmeh Ali, thick settlement layers of up to 3 m date to the Early Chalcolithic period (Fazeli et al., 2004, 2007). Supporting radiocarbon dates are lacking for Cheshmeh Ali, while the uppermost Early Chalcolithic layers at Tappeh Pardis show a time range similar to that of Ahmadabad-e Kuzehgaran. This makes Ajor Pazi an important site, as the TC II is poorly represented in the northern Plateau. TC II dates to the time of the hiatus resulting from the abandonment of the earlier Transitional Chalcolithic period occupation at Tappeh Sialk North and the establishment of an Early Chalcolithic habitation at Tappeh Sialk South. This likely corresponds to the time between the abandonment of Zagheh and the first occupation at Qabrestan in the Qazvin Plain (Fazeli et al., 2005).

4.2 | Holocene paleoenvironmental conditions

Various studies have aimed to understand the Holocene climatic variability in Iran and Central Asia (Jones et al., 2013; Kehl, 2009; Kehl et al., 2023; Schmidt et al., 2011; Shaikh Baikloo Islam, 2020; Staubwasser & Weiss, 2006). Nevertheless, reconstructing the specific paleoenvironmental conditions for the Jajrud drainage basin is challenging due to the poor availability of distinctive

paleoenvironmental archives in the area. The main known aridization and cooling events at about 8.2 and 4.2 ka B.P. are the most drastic global changes in paleoclimatic systems (Staubwasser & Weiss, 2006) and can also be found in the Iranian highlands.

The Qazvin Plain, located ca. 180 km NW of the Varamin Plain, presents a geomorphological setting comparable to that of the Varamin Plain. For the Late Pleistocene and Early Holocene (20–8 ka B.P.), Schmidt et al. (2011) assume predominating sedimentation by sheet flow, which changed to a channelized depositional environment during the Mid-Holocene. For early Mid-Holocene deposits (~7.2 ka B.P.), Schmidt et al. (2011) connect an increase of oak pollen over pistachio pollen in the sediments with a distinctive increase in water availability and coinciding with these favorable environmental conditions, the onset of the new Transitional Chalcolithic pottery style at the archaeological site of Zagheh. These Early to Mid-Holocene environmental changes associated with decreased aridity can also be observed in the Varamin Plain, where in the Mid-Holocene, the proximal parts of the Jajrud alluvial fan were incised as a result of increased runoff, and its distal parts were aggraded (Beaumont, 1972). While it remains unclear how long these relatively humid Mid-Holocene environmental conditions lasted, Schmidt et al. (2011) suggest the onset of a Late-Holocene humid period around 4.3 ka. In contrast, based on speleothem records from Gol-e Zard cave, about 65 km north of Varamin, Carolin et al. (2019) state that there was enhanced dust input around 4.5–4.2 ka B.P.; these findings are interpreted as a consequence of a regional aridization period. Also, records of Lake Mirabad and Zeribar in the Zagros Mountains of western Iran indicate a drought phase beginning at around 5.4 ka B.P. that lasted for about 600 years (Stevens et al., 2006). Age determination of sample OSL-7-APZ (Table 4) also indicates a late Mid-Holocene age. However, explicit examination of the grain-size distributions in the sediments immediately overlying and underlying OSL-7-APZ do not indicate any aeolian depositional processes but rather facies of fluvial sedimentary processes.

4.3 | Holocene depositional processes of the Jajrud fan

The integration of geomorphological and paleoenvironmental data enables us to estimate concomitant conditions that influenced the conditions of occupation at the site of Ajor Pazi and that might have caused the apparent hiatus after 6 ka B.P./ca. 4000 cal. B.C.E. Ajor Pazi is located about 40 km south of the Jajrud fan apex at the distal transition toward the alluvial plain. Sedimentologically, such a transition follows the fan toe like a band and is characterized by sandy sheet flow and braided river sediments (Bowman, 2019; Bull, 1977).

Facies of the exposed sediments at Ajor Pazi document three primary environmental conditions controlling the depositional dynamics:

Facies "a" consists of undifferentiated yellowish fines. Due to the location of the Ajor Pazi site in the distal part of the Jajrud alluvial fan, these unstratified yellowish fines are runoff-controlled and addressed either as flood sediments deposited by a branch of the Jajrud river (Burbank & Anderson, 2012) or as sheet-flow deposits on the slightly inclined surface of the alluvial fan ($\mu = 0.5°$) during torrential rainfall (Beaumont, 1972). However, sheet flow deposits, as well as flood deposits, are typically stratified, including fining-upward cycles (Blair & McPherson, 1994; Bowman, 2019). The lack of clear stratification and the absence of macroscopically discernible fining-upward cycles in facies "a" is explained by a presumably quick deposition. The predominantly fine deposits of facies "a" at the Ajor Pazi site are consistent with the descriptions of Gillmore et al. (2007), referring to the archaeological outcrops at Tappeh Pardis. They interpreted the absence of pebbles as a result of the site's location at the western edge of the fan, which is comparable to the location of the Ajor Pazi site at the transition between the alluvial fan and the plain. Moreover, it cannot be excluded that the delineation of facies "a" is a methodological artifact of the macroscopic description of the sediments due to the short time available in this rescue excavation.

Facies "b" consists of coarse bands of sandy and gravelly material that indicate the occurrence of higher energetic transport processes in the Jajrud's braided river system reaching Ajor Pazi. Typical for these run-off-controlled deposits on alluvial fans are episodic mudflow events (Beaumont, 1972; Bowman, 2019). As mudflow events are linked to the water availability and drainage capacity of the headwater area, the large size of the Jajrud catchment would limit their occurrence. Beaumont (1972) states that mudflows are instead connected to alluvial fans with smaller catchments and, therefore, lower drainage capacities. Deposits in facies "b" show fining upward sequences where the sandy bands are deposited on top of the gravelly layers (Figure 3). These sequences are scattered across all cross-sections and indicate the shifting of channels in a braided system within the distal fan environment (Bowman, 2019; Gillmore et al., 2007).

Facies "c" corresponds to transformed material from facies "a" and "b," The transformation occurred through weathering processes and soil formation as expressed by increased TOC contents (Bahrami & Ghahraman, 2019; Martini & Chesworth, 1992). Beyond that, human impact on the depositional environment must be considered. This includes charcoal as remains from fireplaces (Andam, 2019; Maghsoudi et al., 2014) or due to (quasi-)natural bushfires, which are known to increase in numbers in a settled environment (Andam, 2019), both also increasing TOC contents. Wherever increased TOC contents coincide with higher Rb/K-ratios or χlf-values, we assume that soil formation processes modified the deposits (Profe et al., 2016). However, the usage of χlf-values to distinguish soil formation from fire activities remains uncertain, as high χlf-values might also correspond to ash layers, as documented in Locus 5 in profile B (Sousa et al., 2022).

In *key-profile C* (Figure 4), facies "a" dominates, documented by an overall fine texture. Locally occurring gravel layers corresponding to facies "b" interrupt facies "a" at 90 and 110 cm a.g.s. As displayed by facies "c," soil-formation processes were also observed twice, each time to the upper terminating layers (Unit II and IV), strongly indicating settlement activities. Sediments exposed at the bottom of key-profile C (Units VIII and IX) lack any indication of human

settlement. The sediments are predominantly composed of fines; due to the site's location in the distal part of the Jajrud alluvial fan in the southern Alborz foreland, we assume that the fines were relocated and deposited by aeolian processes as well as by nonconcentrated runoff processes (Blair & McPherson, 1994; Bowman, 2019). Relatively high Al/K-ratios indicate distinct syn-sedimentary chemical weathering activities (Buggle et al., 2011), confirmed by the sediment's slightly brownish color (Jarmer & Schütt, 1998). However, TOC concentrations below 0.3 mass% indicate a lack of soil formation processes. A gravel layer (Unit VII) overlies these banks of homogeneous fines, documenting deposition under a relatively strong current such as triggered by a flood event with the offshoots of the flood wave even reaching the distal parts of the Jajrud alluvial fan and here allowing deposition of gravels (Brookes et al., 1982; Tooth, 2000). The sediment characteristics of Units VIII and IX in key-profile C correspond to those of Unit IV, profile B. In key-profile C, the coarse deposits of Unit VII are overlain by Unit VI, which marks the onset of settlement activities, documented by increased charcoal, sherds, bones, and burnt clay. The artifacts are embedded in a matrix of fines that are similar to those in Unit VIII. However, the only ca. 35-cm-thick Unit VI shows repeated accumulation of gravels such as those during flood events (Brookes et al., 1982; Gillmore et al., 2007, 2011) and their incorporation into the matrix in the settled area. It must be considered that the abundance of ceramics and bone fragments in all samples does not necessarily indicate a continuous settlement of the site, as it might have been caused partly by the relocation of ceramics and bone fragments by runoff processes. However, finds of almost intact pottery, such as a vessel in profile A, indicate an autochthonous character of the archaeological remains. Locus 12, Unit VI shows increased χlf- and χfd-values, which indicates fire activities. In contrast, sediments of overlying Unit V are highly compacted fines and correspond to a (settlement-) surface (Kruse-Peeples et al., 2010). The sequence of fire activities (Locus 12) demonstrates some continuous habitation at the site, while the blanketing layer of compacted fines (Locus 21) possibly indicates an abandonment of Ajor Pazi. However, we could not identify similar sequences or dynamics within the other profiles analyzed. Sediments of the overlying Unit IV are rich in bone fragments and sherds and lack any coarse material; they are homogeneous among all parameters throughout the unit. From these characteristics, we conclude that the 46 cm sediments of Unit IV correspond to overbank deposits, which were most likely accumulated during a single event, including relocated bone fragments and sherds (Saynor & Erskine, 1993). Overlying Unit III, with its high compaction and highly distinct charcoal components, again corresponds to a settlement surface. Toward the top (Units I and II), the depositional environment was similar to that of Unit IV but repeatedly interrupted by flood events with the deposition of coarse-grained sands (Gillmore et al., 2011). We assume that flood events causing such overbank deposits may have led to an abandonment of Ajor Pazi. This assumption also receives confirmation by the decreasing quantities of bone fragments and sherds

toward the top and their total absence in sediments above 230 cm a.g.s. (Unit I). Similar to the sediments of Units IX to III, the uppermost deposits also indicate slight syn-sedimentary chemical weathering processes (Profe et al., 2018).

Sediments with a strong indication of syn-sedimentary settlement activities were also detected in profile B, Units I and II, and in profile F, Units III-XI. The total thickness of layers containing artifacts or proxies indicating settlement activities amount to ca. 110 cm in Profile B and ca. 140 cm in Profile F. As indicated by radiocarbon ages, the onset of settlement activities at the Ajor Pazi site can be dated to ca. 6.4 ka B.P. The lack of radiocarbon dates younger than 5.6 ka B.P. (Table 3) indicates an abandonment of Ajor Pazi, corresponding to the Middle to Late Chalcolithic. Considering the dependency of occupation on access to water, a temporal dislocation of the main drainage on the alluvial fan might have caused the abandonment of Ajor Pazi. Major drivers for a shift of the main discharge could be tectonic movement along the Parchin fault, the outlet of the Jajrud, as well as a change in climatic conditions (Bowman, 2019). For the latter, the amplification of seasonality described by Kirsten and Dallmeyer et al. (2023), compared to only slightly changing mean climatic conditions during the Mid-Holocene could have been influential on the discharge. The study of Pollock et al. (2023) suggests for the Early to Middle Chalcolithic period a shift toward a settlement pattern in the northeastern part of the Varamin Plain. This shift might coincide with the hiatus of settlement at Ajor Pazi and a less suitable environment at the site. The resumed habitation at Ajor Pazi between the Late Chalcolithic and the Bronze Age (Pollock et al., 2023) might suggest continuous access to water and, therefore, rather stable conditions of water availability across the Varamin Plain at that time; however, the numerical dating cannot prove further depositional dynamics.

5 | CONCLUSIONS

Findings regarding local morphodynamics around the site of Ajor Pazi allow for the reconstruction of a Mid-Holocene active fluvial fan environment with repeated channel relocation, overbank flow, and temporary slack-water areas by the nival runoff regime of the Jajrud river. This water-rich environment provided ideal settlement conditions in an arid environment (Kehl et al., 2023). Radiocarbon ages suggest settlement activities at least during 6.4–5.6 ka cal. B.P., with a subsequent hiatus suggested by an absence of cultural remains dating to the Early to Middle Chalcolithic. It can be postulated that relocations of the local effluent stream caused the deterioration of water availability and resulted in the temporary abandonment of the settlement at Ajor Pazi. Likewise, during the absence of settlement, environmental proxies for soil formation also indicate reduced morphodynamics.

AUTHOR CONTRIBUTIONS

Robert Busch: Conceptualization; methodology; software; data curation; visualization; validation; investigation; formal analysis; writing—original draft. **Reinhard Bernbeck**: Conceptualization; investigation; funding acquisition; project administration; supervision; writing–review &

CONFLICT OF INTEREST STATEMENT

The authors declare no conflict of interest.

DATA AVAILABILITY STATEMENT

The data that support the findings of this study are openly available in PANGAEA at https://doi.pangaea.de/10.1594/PANGAEA.961075 [in review].

ORCID

Robert Busch http://orcid.org/0000-0002-6079-7926

REFERENCES

Abbassi, A., Nasrabadi, A., Tatar, M., Yaminifard, F., Abbassi, M. R., Hatzfeld, D., & Priestley, K. (2010). Crustal velocity structure in the Southern edge of the central Alborz (Iran). *Journal of Geodynamics*, 49(2), 68–78.

Adamiec, G., & Aitken, M. J. (1998). Dose-rate conversion factors: Update. *Ancient TL*, 16(2), 37–50.

Ad-hoc-AG Boden (Ed.). (2005). *Bodenkundliche kartieranleitung* (5th ed.). Schweizerbart.

Aitchison, J. (1982). The statistical analysis of compositional data. *Journal of the Royal Statistical Society: Series B (Methodological)*, 44(2), 139–160.

Andam, S. S. G. (2019). *A pedoanthracological and palynological approach to study man-climate-ecosystem interactions during the Holocene in Persepolis basin (SW-Iran)* [Dissertation, Institute of Ecology and Nature Conservation Biology, Universität Regensburg, Regensburg].

Auclair, M., Lamothe, M., & Huot, S. (2003). Measurement of anomalous fading for feldspar IRSL using SAR. *Radiation Measurements*, 37(4–5), 487–492.

Bahrami, S., & Ghahraman, K. (2019). Geomorphological controls on soil fertility of semi-arid alluvial fans: A case study of the Joghatay Mountains, Northeast Iran. *Catena*, 176, 145–158.

Barge, L. M., Flores, E., VanderVelde, D. G., Weber, J. M., Baum, M. M., & Castonguay, A. (2020). Effects of geochemical and environmental parameters on abiotic organic chemistry driven by iron hydroxide minerals. *Journal of Geophysical Research: Planets*, 125(11): e2020JE006423.

Beaumont, P. (1968). Qanats on the Varamin Plain, Iran. *Transactions of the Institute of British Geographers*, 45, 169–179.

Beaumont, P. (1972). Alluvial fans along the foothills of the Elburz Mountains, Iran. *Palaeogeography, Palaeoclimatology, Palaeoecology*, 12(4), 251–273.

Beaumont, P. (1974). Water resource development in Iran. *The Geographical Journal*, 140(3), 418–431.

Bernbeck, R., Hessari, M., Pollock, S., Rol, N., & Akbari, H. (2020). Soundings at three chalcolithic sites in the varamin plain, 2018. *Archäologische Mitteilungen aus Iran und Turan No*, 49, 49–75.

Blair, T. C., & McPherson, J. G. (1994). Alluvial fan processes and forms. In A. D. Abrahams & A. J. Parsons (Eds.), *Geomorphology of desert environments* (pp. 354–402). Springer.

Blum, P. (1997). *Physical properties handbook: A guide to the shipboard measurement of physical properties of deep-sea cores* (Vol. 26). Ocean Drilling Program Tech Note.

van den Boogaart, K. G., & Tolosana-Delgado, R. (2008). "Compositions": A unified R package to analyze compositional data. *Computers & Geosciences*, 34(4), 320–338.

Bordbar, M. (1967), *Notice Explicative de la carte pedologique de Varamine (Province Centrale) Iran, Comme la rapport de stage pedologique*.

Bowman, D. (2019). *Principles of alluvial fan morphology* (1st ed.). Springer.

Bronk Ramsey, C. (1995). Radiocarbon calibration and analysis of stratigraphy: The OxCal program. *Radiocarbon*, 37(2), 425–430.

Brookes, I. A., Levine, L. D., & Dennell, R. W. (1982). Alluvial sequence in central west Iran and implications for archaeological survey. *Journal of Field Archaeology*, 9(3), 285–299.

Buggle, B., Glaser, B., Hambach, U., Gerasimenko, N., & Marković, S. (2011). An evaluation of geochemical weathering indices in loess–paleosol studies. *Quaternary International*, 240(1–2), 12–21.

Bull, W. B. (1977). The alluvial-fan environment. *Progress in Physical Geography: Earth and Environment*, 1(2), 222–270.

Burbank, D. W., & Anderson, R. S. (2012). *Tectonic geomorphology* (2nd ed.). Wiley-Blackwell.

Buylaert, J.-P., Jain, M., Murray, A. S., Thomsen, K. J., Thiel, C., & Sohbati, R. (2012). A robust feldspar luminescence dating method for Middle and Late Pleistocene sediments. *Boreas*, 41(3), 435–451.

Buylaert, J.-P., Murray, A. S., Thomsen, K. J., & Jain, M. (2009). Testing the potential of an elevated temperature IRSL signal from K-feldspar. *Radiation Measurements*, 44(5–6), 560–565.

Bøtter-Jensen, L., Andersen, C. E., Duller, G. A. T., & Murray, A. S. (2003). Developments in radiation, stimulation and observation facilities in luminescence measurements. *Radiation Measurements*, 37(4–5), 535–541.

Bøtter-Jensen, L., Bulur, E., Duller, G. A. T., & Murray, A. S. (2000). Advances in luminescence instrument systems. *Radiation Measurements*, 32(5–6), 523–528.

Bøtter-Jensen, L., Thomsen, K. J., & Jain, M. (2010). Review of optically stimulated luminescence (OSL) instrumental developments for retrospective dosimetry. *Radiation Measurements*, *45*(3–6), 253–257.

Carolin, S. A., Walker, R. T., Day, C. C., Ersek, V., Sloan, R. A., Dee, M. W., Talebian, M., & Henderson, G. M. (2019). Precise timing of abrupt increase in dust activity in the Middle East coincident with 4.2 ka social change. *Proceedings of the National Academy of Sciences of the United States of America*, *116*(1), 67–72.

Chiverrell, R. C., Thorndycraft, V. R., & Hoffmann, T. O. (2011). Cumulative probability functions and their role in evaluating the chronology of geomorphological events during the Holocene. *Journal of Quaternary Science*, *26*(1), 76–85.

Core Team R. (2013). *R: A language and environment for statistical computing*. R Foundation for Statistical Computing.

Dearing, J. A. (1999). *Environmental magnetic susceptibility: Using the Bartington MS2 system* (2nd ed). Chi Publisher.

Fazeli, H., Coningham, R. A. E., & Batt, C. M. (2004). Cheshmeh-Ali revisited: Towards an absolute dating of the late neolithic and chalcolithic of Iran's Tehran plain. *Iran*, *42*, 13–23.

Fazeli, H., Coningham, R. A. E., Young, R. L., Gillmore, G. K., Maghsoudi, M., & Raza, H. (2007). Socio-economic transformations in the Tehran plain: Final season of settlement survey and excavations at tepe pardis. *Iran*, *45*(1), 267–285.

Fazeli, H., Wong, E. H., & Potts, D. T. (2005). The Qazvin plain revisited. *Ancient Near Eastern Studies*, *42*, 3–82.

Feng, Z.-D. (1997). Geochemical characteristics of a Loess-soil sequence in central kansas. *Soil Science Society of America Journal*, *61*(2), 534–541.

Galbraith, R. F., Roberts, R. G., Laslett, G. M., Yoshida, H., & Olley, J. M. (1999). Optical dating of single and multiple grains of quartz from Jinmium rock shelter, northern Australia: Part I, experimental design and statistical models. *Archaeometry*, *41*(2), 339–364.

Ghasemi, S., Hessari, M., & Akbari, H. (2018). Zavarehvar, the central site from of the urbanization period (Protoliterate) of varamin plain: studying pottery features. *Parseh Journal of Archaeological Studies*, *2*(4), 51–68.

Gillmore, G. K., Coningham, R. A. E., Young, R. L., Fazeli, H. N., Rushworth, G., Donahue, R., & Batt, C. M. (2007). Holocene alluvial sediments of the Tehran Plain: Sedimentation and archaeological site visibility. In L. Wilson, P. Dickinson, & J. Jeandron (Eds.), *Reconstructing human-landscape interactions* (pp. 37–67). Cambridge Scholars Publishing.

Gillmore, G. K., Stevens, T., Buylaert, J. P., Coningham, R. A. E., Batt, C., Fazeli, H., Young, R., & Maghsoudi, M. (2011). Geoarchaeology and the value of multidisciplinary palaeoenvironmental approaches: A case study from the Tehran plain, Iran. *Geological Society, London, Special Publications*, *352*(1), 49–67.

Hessari, M., Akbari, H., Muradsultan, M. S., Moezizareh, S. M., & Ghasemi, S. (2014). Survey of Southern Pishva, Javadabad District, Tehran Province. *Reports of the 13th annual symposium on the Iranian Archaeology* [in Persian], Tehran, 107–109.

Huntley, D. J., & Baril, M. R. (1997). The K content of the K-feldspars being measured in optical dating or in thermoluminescence dating. *Ancient TL*, *15*(1), 11–13.

Huntley, D. J., & Lamothe, M. (2001). Ubiquity of anomalous fading in K-feldspars and the measurement and correction for it in optical dating. *Canadian Journal of Earth Sciences*, *38*(7), 1093–1106.

Jackson, J. (2006). Fatal attraction: Living with earthquakes, the growth of villages into megacities, and earthquake vulnerability in the modern world. *Philosophical Transactions of the Royal Society A: Mathematical, Physical and Engineering Sciences*, *364*(1845), 1911–1925.

Jamshidi, M., Tajrishy, M., & Maghrebi, M. (2010). Modeling of point and non-point source pollution of nitrate with SWAT in the Jajrood river watershed, Iran. *International Agricultural Engineering Journal*, *19*(2), 23–31.

Jarmer, T., & Schütt, B. (1998). Analysis of iron contents in carbonate bedrock by spectroradiometric detection based on experimentally designed substrates. In *1st EARSeL workshop on imaging spectroscopy*, Remote Sensing Laboratories, pp. 375–382.

Jolliffe, I. T. (2002). *Principal component analysis, Springer series in statistics* (2nd ed.). Springer.

Jones, M., Djamali, M., Stevens, L. R., Heyvaert, V., Askari, H., Noorollahi, D., & Weeks, L. (2013). Mid-Holocene environmental and climatic change in Iran. In C. A. Petrie & J. R. Alden (Eds.), *Ancient Iran and its neighbours: Local developments and long-range interactions in the fourth millennium BC, British Institute of Persian Studies archaeological monographs series* (pp. 25–34). Oxbow Books.

Kassambara, A., & Mundt, F. (2020), *factoextra: Extract and visualize the results of multivariate data analyses, R Package Version 1.0.7*, https://CRAN.R-project.org/package=factoextra

Kehl, M. (2009). Quaternary climate change in Iran: The state of knowledge. *Erdkunde*, *63*(1), 1–17.

Kehl, M., Rafiei-Alavi, B., & Lahijani, H. (2023). Holocene paleoenvironmental change and phases of drought in the Iranian Highlands. A review. In R. Bernbeck, S. Pollock, & G. Eberhardt (Eds.), *Coming to terms with the future: Concepts of resilience for the study of early Iranian societies*. Sidestone Press.

Khormali, F., & Toomanian, N. (2018). Soil-forming factors and processes. In M.-Ḥ. Rūzītalab, H. Siadat & A. Farshad (Eds.), The soils of Iran, World soils book series (pp. 73–91). Springer.

Kirsten, F., Dallmeyer, A., Bernbeck, R., Böhmer, T., Busch, R., Hessari, M., Pollock, S., & Schütt, B. (2023). Were climatic forcings the main driver for mid-holocene changes in settlement dynamics on the Varamin Plain (Central Iranian Plateau)?. *PLOS ONE*, *18*(10), e0290181. https://doi.org/10.1371/journal.pone.0290181

Knitter, D., Bernbeck, R., Schier, W., & Schütt, B. (2021). Introduction: Reflections on the applicability of a social ecological concept to research in a framework of spatial environment and conceptual design. In D. Knitter, W. Schier & B. Schütt, (Eds.), *The concept of social ecology as a means to integrate humanities and science in landscape archaeological research* (pp. 7–36). Edition Topoi.

Krbetschek, M. R., Götze, J., Dietrich, A., & Trautmann, T. (1997). Spectral information from minerals relevant for luminescence dating. *Radiation Measurements*, *27*(5–6), 695–748.

Kreutzer, S., Schmidt, C., Fuchs, M. C., Dietze, M., Fischer, M., & Fuchs, M. (2012). Introducing an R package for luminescence dating analysis. *Ancient TL*, *30*(1), 1–8.

Kruse-Peeples, M., Schaafsma, H., Briggs, J. M., & Spielmann, K. A. (2010). Landscape legacies of prehistoric agricultural land use in the Perry Mesa region, central Arizona. *The Archaeology of Anthropogenic Environments, Occasional Paper No*, *37*, 122–141.

Kulig, G. (2005). *Erstellung einer Auswertesoftware zur Altersbestimmung mittels Lumineszenzverfahren unter spezieller Berücksichtigung des Einflusses radioaktiver Ungleichgewichte in der 238U-Zerfallsreihe* [B.Sc. thesis, Technische Universität Bergakademie] Freiberg.

Lüthgens, C., Neuhuber, S., Grupe, S., Payer, T., Peresson, M., & Fiebig, M. (2017). Geochronological investigations using a combination of luminescence and cosmogenic nuclide burial dating of drill cores from the Vienna Basin. *Zeitschrift der Deutschen Gesellschaft für Geowissenschaften*, *168*(1), 115–140.

Maghrebi, M., Tajrishy, M., & Jamshidi, M. (2010). Assessment of Jajrood river watershed microbial pollution: Sources and fates. *Environmental Engineering & Management Journal (EEMJ)*, *9*(3), 385–391.

Maghsoudi, M., Simpson, I. A., Kourampas, N., & Nashli, H. F. (2014). Archaeological sediments from settlement mounds of the Sagzabad Cluster, central Iran: Human-induced deposition on an arid alluvial plain. *Quaternary International*, *324*, 67–83.

Martini, I. P., & Chesworth, W. (Eds.). (1992). *Weathering, soils & paleosols, developments in earth surface processes* (Vol. 2). Elsevier.

Meder, O. (1979). *Klimaökologie und Siedlungsgang auf dem Hochland von Iran in vor- und frühgeschichtlicher Zeit* (Vol. 80). Marburger Geographische Schriften.

Mejdahl, V. (1979). Thermoluminescence dating: Beta-dose attenuation in quartz grains. *Archaeometry*, 21(1), 61–72.

Menne, M. J., Durre, I., Korzeniewski, B., McNeill, S., Thomas, K., Yin, X., Anthony, S., Ray, R., Vose, R. S., Gleason, B. E., & Houston, T. G. (2012), *Global historical climatology network: Daily (GHCN-Daily), Version 3*, NOAA National Centers for Environmental Information.

Murray, A. S., Thomsen, K. J., Masuda, N., Buylaert, J.-P., & Jain, M. (2012). Identifying well-bleached quartz using the different bleaching rates of quartz and feldspar luminescence signals. *Radiation Measurements*, 47(9), 688–695.

Otto, N. (2022). *Analyse der Gerinnedynamiken zwischen 1969/70 und 2021 auf dem östlichen Teil des Jajrud-Schwemmfächers, südliches Elburs Vorland/Iran* [unpublished bachelor thesis]. Freie Universität Berlin.

Pollard, M., Fazeli, H. N., Davoudi, H., Sarlak, S., Helwing, B., & Saeidi, F. (2013). A new radiocarbon chronology for the North Central Plateau of Iran from the Late Neolithic to the Iron Age. *Archäologische Mitteilungen aus Iran und Turan*, 45, 27–50.

Pollock, S., Hessari, M., & Bernbeck, R. (2023). Reaching the breaking point? Developments in the chalcolithic to early Bronze Age Varamin plain. In R. Bernbeck, S. Pollock, & G. Eberhardt (Eds.), *Coming to terms with the future: Concepts of resilience for the study of early Iranian Societies*. Sidestone Press.

Prescott, J. R., & Hutton, J. T. (1994). Cosmic ray contributions to dose rates for luminescence and ESR dating: Large depths and long-term time variations. *Radiation Measurements*, 23(2–3), 497–500.

Prescott, J. R., & Stephan, L. G. (1982). The contribution of cosmic radiation to the environmental dose for thermoluminescence. Latitude, altitude and depth dependences. *TLS*, 1, 16–25.

Profe, J., Wacha, L., Frechen, M., Ohlendorf, C., & Zolitschka, B. (2018). XRF scanning of discrete samples – A chemostratigraphic approach exemplified for loess-paleosol sequences from the Island of Susak, Croatia. *Quaternary International*, 494, 34–51.

Profe, J., Zolitschka, B., Schirmer, W., Frechen, M., & Ohlendorf, C. (2016). Geochemistry unravels MIS 3/2 paleoenvironmental dynamics at the loess–paleosol sequence Schwalbenberg II, Germany. *Palaeogeography, Palaeoclimatology, Palaeoecology*, 459, 537–551.

Rades, E. F., Fiebig, M., & Lüthgens, C. (2018). Luminescence dating of the Rissian type section in Southern Germany as a base for correlation. *Quaternary International*, 478, 38–50.

Razmkhah, H., Abrishamchi, A., & Torkian, A. (2009). Evaluation of spatial and temporal variation in water quality by pattern recognition techniques: A case study on Jajrood River (Tehran, Iran). *Journal of Environmental Management*, 91(4), 852–860.

Reimer, P. J., Austin, W. E. N., Bard, E., Bayliss, A., Blackwell, P. G., Bronk Ramsey, C., Butzin, M., Cheng, H., Edwards, R. L., Friedrich, M., Grootes, P. M., Guilderson, T. P., Hajdas, I., Heaton, T. J., Hogg, A. G., Hughen, K. A., Kromer, B., Manning, S. W., Muscheler, R., … Talamo, S. (2020). The IntCal20 Northern Hemisphere radiocarbon age calibration curve (0–55 cal kBP). *Radiocarbon*, 62(4), 725–757.

Ridder, N. A. de, & Erez, A. (1977), *Optimum use of water resources*, Wageningen.

Rieben, H. (1955). The geology of the Teheran plain. *American Journal of Science*, 253, 617–639.

Rol, N., Bernbeck, R., Wolff-Heger, L., Akbari, H., Hessari, M., Pollock, S., & Schäfer, D. (2022). Chalcolithic painted pottery of the Sialk III period:

Quantifying stylistic continuities and changes on the Northern central plateau. *Journal of the British Institute of Persian Studies*, 1, 1–22.

Sadeghi, A., & Fondoudi, M. (2006), *Geological map of Iran: Varamin*, Sheet NO. 6360, Geological Survey & Mineral Exploration of Iran.

Saynor, M., & Erskine, W. (1993). Characteristics and implications of high-level slackwater deposits in the Fairlight Gorge, Nepean River, Australia. *Marine and Freshwater Research*, 44(5), 735–747.

Schmidt, A., Quigley, M., Fattahi, M., Azizi, G., Maghsoudi, M., & Fazeli, H. (2011). Holocene settlement shifts and palaeoenvironments on the Central Iranian plateau: Investigating linked systems. *The Holocene*, 21(4), 583–595.

Schulte, P., Lehmkuhl, F., Steininger, F., Loibl, D., Lockot, G., Protze, J., Fischer, P., & Stauch, G. (2016). Influence of HCl pretreatment and organo-mineral complexes on laser diffraction measurement of loess–paleosol-sequences. *Catena*, 137, 392–405.

Scrucca, L., Fop, M., Murphy, T. B., & Raftery, E. (2016). mclust 5: Clustering, classification and density estimation using Gaussian finite mixture models. *The R Journal*, 8(1), 289–317.

Shaikh Baikloo Islam, B. (2020). Holocene climatic events in Iran. *Journal of Climate Change Research*, 1(4), 35–47.

de Sousa, D. V., Rodet, M. J., Duarte-Talim, D., Teixeira, W. G., Prous, A., Vasconcelos, B. N., & Pereira, E. (2022). Linking anthropogenic burning activities to magnetic susceptibility: Studies at Brazilian archaeological sites. *Geoarchaeology*, 38(1), 89–108.

Staubwasser, M., & Weiss, H. (2006). Holocene climate and cultural evolution in late prehistoric–early Historic West Asia. *Quaternary Research*, 66(3), 372–387.

Stevens, L. R., Ito, E., Schwalb, A., & Wright, H. E. (2006). Timing of atmospheric precipitation in the Zagros mountains inferred from a Multi-proxy record from Lake Mirabad, Iran. *Quaternary Research*, 66(3), 494–500.

Tjallingii, R., Röhl, U., Kölling, M., & Bickert, T. (2007). Influence of the water content on X-ray fluorescence core-scanning measurements in soft marine sediments. *Geochemistry, Geophysics, Geosystems*, 8(2), 2006GC001393.

Tooth, S. (2000). Process, form and change in dryland rivers: A review of recent research. *Earth-Science Reviews*, 51(1–4), 67–107.

Valipour, M., Krasilnikof, J., Yannopoulos, S., Kumar, R., Deng, J., Roccaro, P., Mays, L., Grismer, M. E., & Angelakis, A. N. (2020). The evolution of agricultural drainage from the earliest times to the present. *Sustainability*, 12(1), 416.

Wintle, A. G. (1973). Anomalous fading of thermo-luminescence in mineral samples. *Nature*, 245(5421), 143–144.

SUPPORTING INFORMATION

Additional supporting information can be found online in the Supporting Information section at the end of this article.